Pergamon

PII: S0016-2361(96)00087-0

Int. J. Multiphase Flow Vol. 23, No. 3, pp. 575–605, 1997

Printed in Great Britain
0301-9322/97 $17.00 + 0.00

NUMERICAL SIMULATION OF DILUTE TURBULENT GAS–SOLID FLOWS IN HORIZONTAL CHANNELS

C. K. K. LUN and H. S. LIU

Department of Engineering, Dalhousie University, Halifax, NS, B3H 3J5, Canada

(Received 6 March 1996; in revised form 24 November 1996)

Abstract—A dilute turbulent gas–solid two-phase flow model is developed in the present study. Time-averaged conservation equations for mass and momentum, and a two-equation k–ϵ closure are used to model the fluid phase. The solid phase consisting of inelastic, frictional, uniform spheres is simulated by using a Lagrangian approach in which the particle trajectories and velocities are determined by integrating the particle equations of motion. The fluid–solid coupling effects due to solid volume fraction and interfacial momentum interaction are incorporated in the simulation. A sticking–sliding collision model is employed for the particle–particle collisions and the particle–wall collisions. The two-phase model is implemented to simulate gas–solid suspensions in a horizontal channel. Substantial agreement is found between the simulation result and the experimental data for the fluid pressure gradient, the distributions of mean gas velocity, mean particle velocity and concentration. For dilute systems with solids volume fraction of the order 10^{-3}, interparticle collisions are found to be crucial in sustaining a steady and fully developed suspension in the horizontal channel, while the Magnus lift due to particle rotation is found to play a significant role as well. Detailed new numerical results for macroscopic properties such as Reynolds stresses, air turbulence intensities, particle fluctuation kinetic energy, mean particle angular velocity, particle stresses and angular momentum fluxes are presented in the paper. © 1997 Elsevier Science Ltd. All rights reserved.

Key Words: gas–solid suspensions, turbulence, particle rotation, stresses

1. INTRODUCTION

Turbulent gas–solid flows are widely encountered in nature and industrial processes; for example, sand storm, powder snow avalanche, pneumatic transport of particulate, cyclone separators and classifiers, chemical reactors, and fluidized beds to name a few. These systems often involve complicated flow dynamics and interactions between flow constituents and their surroundings.

Experimental and numerical studies of gas–solid suspensions with relatively large particles in pipes or channels had been conducted by researchers such as Lourenco *et al.* (1983), Tsuji *et al.* (1982, 1987) and Frank *et al.* (1993). Empirical power law (Frank *et al.* 1993), logarithmic law of wall (Oesterle and Petitjean 1993), a single boundary layer equation expressed in terms of a stream function (Tsuji *et al.* 1987), one-equation eddy viscosity model (Lourenco *et al.* 1983), two-equation k–ϵ scheme (Sommerfeld 1992) had been used to model the fluid phase. All the above numerical simulations except one, used one-way coupling in which the influence of the solid particles on the fluid phase is neglected. Tsuji *et al.* (1987) incorporated in their model a two-way coupling in interfacial momentum interaction. A number of experimental measurements of mean fluid velocity profile in horizontal pipes and channels have shown that the fluid velocity profiles could be significantly modified by the interfacial coupling effect even at very dilute systems with bulk solids volume fraction of the order 10^{-3}.

Interparticle collisions are often neglected in simulation studies of dilute gas–solid suspension such as in Tsuji *et al.* (1987), Sommerfeld (1992) and Frank *et al.* (1993). Oesterle and Petitjean (1993) incorporated interparticle collisions of inelastic, frictional spheres in their 'non-dilute' gas–solid suspension in a horizontal pipe by randomly generating artificial particle–particle collisions according to an *ad hoc* collision probability distribution which was derived from a local Maxwellian distribution.

Particle–wall collisions play an integral role in gas–solid wall-bounded flow systems. Lourenco *et al.* (1983), Tsuji *et al.* (1987), Sommerfeld (1992) and Frank *et al.* (1993) had proposed similar kind of 'virtual wall' model to account for the effect of 'wall roughness'. Typically, the angles of

reflection or the collisional properties of the impinging particles were changed randomly within certain limits associated with a virtual wall. Using a traditional rigid-body-dynamics model for inelastic, frictional particle–wall collisions, Tsuji *et al.* (1987) found in their numerical simulation that the individual particle eventually deposited on the bottom of the horizontal channel, while their experiments apparently showed a steady suspension. When a virtual wall model was employed in their simulation, the bouncing motion of individual particle was sustained, and collectively the particles constituted a steady flow. One obvious function of a virtual wall was to redirect particle momentum randomly each time a particle collided with the wall. The horizontal streamwise impulse is often greater than the vertical one. As far as large spherical particles colliding with solid flat walls are concerned, the virtual wall model could have acted essentially as an *artificial* momentum source for the solid phase in the vertical direction. As a result, the vertical velocity component of the dispersed phase is increased, and particle deposition is avoided. In view of this, it is perhaps fair to say that at the present time the fundamental mechanism of how the particles are suspended in a horizontal turbulent fluid–solid flow is still not well understood.

In this paper, a dilute turbulent gas–solid two-phase model is proposed. The turbulent gas phase is modeled by a set of time-averaged conservation equations for mass and momentum, and a two-equation k–ϵ closure. The solid phase consisting of inelastic, frictional, uniform spherical particles is simulated by using a Lagrangian approach in which the particle trajectories and velocities are calculated by integrating the equations of motion for particles dispersed in a turbulent fluid. A sticking–sliding collision model (Lun and Bent 1994) is employed for the particle–particle collisions and the particle–wall collisions. A two-way coupling iterative scheme is used to account for the coupling effects of solids volume fraction and interfacial momentum interaction. The two-phase model is applied to simulate a dilute turbulent gas–solid flow in a horizontal channel in which the fundamental flow governing mechanisms are examined. The simulation result is compared with experimental data.

2. FLUID-PHASE TRANSPORT EQUATIONS

The fluid-phase is assumed to be isothermal and incompressible. The volume fraction of the solid phase is defined as $\alpha = nV_p/V_c$, where V_p is the volume of a single particle and n is the number of particles in the volume V_c. A dilute flow system with $\alpha < 0.1$ is considered here.

Crowe (1982) proposed that a dilute gas-particle flow is a flow in which the particle motion is controlled by local aerodynamic forces, and in a dense gas-particle flow, particle motion is governed by particle–particle collisions. Elghobashi (1994) distinguished dilute systems from dense ones based upon particle volume fraction and the ratio of the particle response time to the turbulent timescale. He suggested that systems with $\alpha < 0.001$ are dilute and those with $\alpha > 0.001$ are dense. According to the kinetic theory and the numerical simulations of gravity-free simple shear flows of single solid phase granular materials (Lun *et al.* 1984; Lun and Bent 1994), systems with $\alpha < 0.1$ can be regarded as dilute where the dominant mechanism for energy and momentum transfer is the kinetic mode rather than the collisional one.

By focusing on a small finite control volume in the suspension, the mass conservation for the fluid phase may be expressed as

$$\frac{\partial}{\partial t}(\beta\rho_f) + \frac{\partial}{\partial x_i}(\beta\rho_f u_i) = 0 \qquad [1]$$

where ρ_f and $\beta = 1 - \alpha$ are the mass density and the volume fraction of the fluid phase, respectively. The instantaneous fluid velocity $\mathbf{u}$ is the sum of a mean component $\mathbf{U}$ and a fluctuation component $\mathbf{u}'$, i.e. $\mathbf{u} = \mathbf{U} + \mathbf{u}'$. (Lower case letters or symbols, upper case ones and primed lower case ones denote instantaneous, mean, and fluctuation quantities, respectively, unless specified otherwise.) Similarly, the momentum conservation for the fluid phase may be written as

$$\frac{\partial}{\partial t}(\beta\rho_f u_i) + \frac{\partial}{\partial x_j}(\beta\rho_f u_j u_i) = -\frac{\partial}{\partial x_i}(\beta p) + \frac{\partial}{\partial x_j}(\beta\sigma_{ij}) - m_i + \rho_f\beta g_i \qquad [2]$$

where p is the fluid pressure and $\boldsymbol{g}$ is the gravitational acceleration. The fluid stress tensor σ_{ij} is given as

$$\sigma_{ij} = \mu\left(\frac{\partial u_i}{\partial x_j} + \frac{\partial u_j}{\partial x_i}\right) - \frac{2}{3}\mu\frac{\partial u_k}{\partial x_k}\delta_{ij} \qquad [3]$$

where μ is the fluid dynamic viscosity and δ_{ij} is the unit tensor. The quantity $\mathbf{m}$ in [2] is the interfacial momentum flux per unit volume inside the control volume V_c. If the forces acting on each particle within V_c are known, then one has

$$\mathbf{m} = \frac{1}{V_c}\sum_{j=1}^{n}\mathbf{F}_j \qquad [4]$$

where $\mathbf{F}_j$ is the net fluid force exerting upon the jth particle. Note that the definition of $\mathbf{m}$ in [4] is analogous to that of solids volume fraction and they both are volumetric mean quantities.

The Reynolds time-averaging method is applied to [1]–[2]. Flows with relatively large and massive particles moving at intermediate particle Reynolds number in the inertia regime are considered in the present study. The particle Reynolds number, $\mathrm{Re}_p = \rho_f v_r d/\mu$, is of the order 10^2 where d is the particle diameter of the order 10^{-3} m, μ is the fluid viscosity, and v_r is the relative velocity between the particle and the local fluid. The gas to solid density ratio, ρ_f/ρ_p, is of the order 10^{-3}. The ratio of the particle response time to the eddy turnover time is

$$\frac{\tau_p}{\tau_e} = \frac{4}{3C_D}\left(\frac{\rho_p}{\rho_f}\right)\left(\frac{u_e}{v_r}\right)\left(\frac{d}{\lambda_e}\right).$$

The factor $4/(3C_D)$, and the ratios u_e/v_r and d/λ_e are approximately of order unity; C_D is the drag coefficient, u_e and λ_e are the characteristic velocity and lengthscale of the large eddies, respectively. As a result, the ratio τ_p/τ_e is roughly of the order 10^3. Thus, the influence of fluid turbulence on the particles' motion would be small. The fluctuations of the particle properties, ψ_p', and those of the fluid properties, ϕ_f', may be assumed to be uncorrelated, i.e. $\overline{\psi_p'\phi_f'} = 0$. Quantities with overbars denote time-averaged values. Furthermore, the volumetric mean quantities of the solid phase such as the volume fraction and the interfacial momentum flux per unit volume ($\mathbf{m}$) are assumed to *independent* of the turbulence averaging time-scale of the fluid phase. In other words, we have taken $\bar{\alpha}' = 0$ and $\bar{\alpha} = \alpha$, and similarly $\bar{\mathbf{m}}' = 0$ and $\bar{\mathbf{m}} = \mathbf{M}$. As a result, from [1] the time-averaged continuity equation for the fluid phase is

$$\frac{\partial}{\partial t}(\beta\rho_f) + \frac{\partial}{\partial x_i}(\beta\rho_f U_i) = 0. \qquad [5]$$

Similarly, the time-averaged momentum equation is

$$\frac{\partial}{\partial t}(\beta\rho_f U_i) + \frac{\partial}{\partial x_i}(\beta\rho_f U_j U_i) = \frac{\partial}{\partial x_i}(\beta P) + \frac{\partial}{\partial x_j}[\beta(\tau_{ij} + \tau_{ij}')] - M_i + \rho_f\beta g_i \qquad [6]$$

where the mean fluid stress tensor is

$$\tau_{ij} = \mu\left(\frac{\partial U_i}{\partial x_j} + \frac{\partial U_j}{\partial x_i}\right) - \frac{2}{3}\mu\frac{\partial U_k}{\partial x_k}\delta_{ij}$$

and $\tau_{ij}' = -\rho_f\overline{u_i' u_j'}$ is the Reynolds stress tensor.

In conjunction with a single-phase fluid k–ϵ turbulent model, Nisizima and Yoshizawa (1987) proposed an anisotropic Reynolds stress tensor as follows,

$$\tau'_{ij} = -\frac{2}{3}\rho_f k\delta_{ij} + \mu_t\left(\frac{\partial U_i}{\partial x_j} + \frac{\partial U_j}{\partial x_i}\right) + \frac{\rho_f}{3}\left(\sum_{m=1}^{3}\tau_m S_{mkk}\right)\delta_{ij} - \rho_f\sum_{m=1}^{3}\tau_m S_{mij} \quad [7]$$

and

$$\tau_m = C_{\tau m}k^3/\epsilon^2$$

$$S_{1ij} = \frac{\partial U_i}{\partial x_k}\frac{\partial U_j}{\partial x_k}$$

$$S_{2ij} = \frac{1}{2}\left(\frac{\partial U_i}{\partial x_k}\frac{\partial U_k}{\partial x_j} + \frac{\partial U_j}{\partial x_k}\frac{\partial U_k}{\partial x_i}\right)$$

$$S_{3ij} = \frac{\partial U_k}{\partial x_i}\frac{\partial U_k}{\partial x_j}$$

where $C_{\tau m}$ (subscript $m = 1, 2, 3$) are model coefficients. According to Nisizima and Yoshizawa, the turbulence intensities in channel flows may be written as

$$\overline{u_x'^2} = \frac{2}{3}k + \frac{1}{3}(2C_{\tau 1} - C_{\tau 3})\frac{k^3}{\epsilon^2}\left(\frac{\partial U_x}{\partial y}\right)^2 \quad [8a]$$

$$\overline{u_y'^2} = \frac{2}{3}k - \frac{1}{3}(C_{\tau 1} - 2C_{\tau 3})\frac{k^3}{\epsilon^2}\left(\frac{\partial U_x}{\partial y}\right)^2 \quad [8b]$$

$$\overline{u_z'^2} = \frac{2}{3}k - \frac{1}{3}(C_{\tau 1} + C_{\tau 3})\frac{k^3}{\epsilon^2}\left(\frac{\partial U_x}{\partial y}\right)^2 \quad [8c]$$

where the coefficients $C_{\tau 1} = 0.07$ and $C_{\tau 3} = -0.015$ were obtained by optimizing the agreement between the numerical predictions and the measurements for turbulent intensities in channel flows. The coefficient $C_{\tau 2}$ which was not involved in the channel flow analysis remains an unknown.

The turbulent kinetic energy, k, and the rate of turbulent kinetic energy dissipation, ϵ, are defined as

$$k = \overline{u_i' u_i'}/2$$

and

$$\epsilon = \nu\overline{\frac{\partial u_i'}{\partial x_j}\frac{\partial u_i'}{\partial x_j}}$$

respectively, where ν is the fluid kinematic viscosity. The turbulent eddy viscosity μ_t in [7] may be expressed as

$$\mu_t = \rho_f C_\mu \frac{k^2}{\epsilon} \quad [9]$$

where C_μ is a constant (Launder and Spalding 1974).

The turbulent kinetic energy equation and the rate of turbulent kinetic energy dissipation equation can be derived by taking moment of $\mathbf{u}'$ with the instantaneous momentum equation [2] and moment of $\nu\nabla\mathbf{u}'$ with the gradient of the instantaneous momentum equation [2], respectively.

After applying time-averaging to the equations and modeling various terms in a manner similar to that performed for a single-phase turbulent fluid, the k–ϵ equations for fluid–solid flows are

$$\frac{\partial}{\partial t}(\beta\rho_f k) + \frac{\partial}{\partial x_j}(\beta\rho_f U_j k) = \frac{\partial}{\partial x_j}\left[\beta\left(\mu + \frac{\mu_t}{\sigma_k}\right)\frac{\partial k}{\partial x_j}\right] + \beta\tau'_{ij}\frac{\partial U_i}{\partial x_j} - \beta\rho_f\epsilon \qquad [10]$$

and

$$\frac{\partial}{\partial t}(\beta\rho_f\epsilon) + \frac{\partial}{\partial x_j}(\beta\rho_f U_j\epsilon) = \frac{\partial}{\partial x_j}\left[\beta\left(\mu + \frac{\mu_t}{\sigma_\epsilon}\right)\frac{\partial\epsilon}{\partial x_j}\right] + C_{\epsilon 1}\beta\frac{\epsilon}{k}\tau'_{ij}\frac{\partial U_i}{\partial x_j} - C_{\epsilon 2}\beta\rho_f\frac{\epsilon^2}{k}. \qquad [11]$$

In deriving [10]–[11], the fluid fluctuation energy per unit volume ($\overline{u'_i m'_i}$) and the energy dissipation rate

$$\left(2\nu\overline{\frac{\partial u'_i}{\partial x_k}\frac{\partial m'_i}{\partial x_k}}\right)$$

due to the interfacial momentum transfer per unit volume are assumed to be negligibly small.

If the fluid volume fraction β in [10]–[11] is equated to unity, the k–ϵ equations reduce to those derived by Launder and Spalding (1974) for a single-phase turbulent fluid. In dilute systems such as the ones addressed in the present study where the ratio $\tau_p/\tau_e \gg 1$, the degree of *direct* turbulence modulation in the carrier fluid due to the wakes shed by the relatively large and massive particles will be insignificant. The adoption of the closure coefficients from the single-phase k–ϵ turbulence

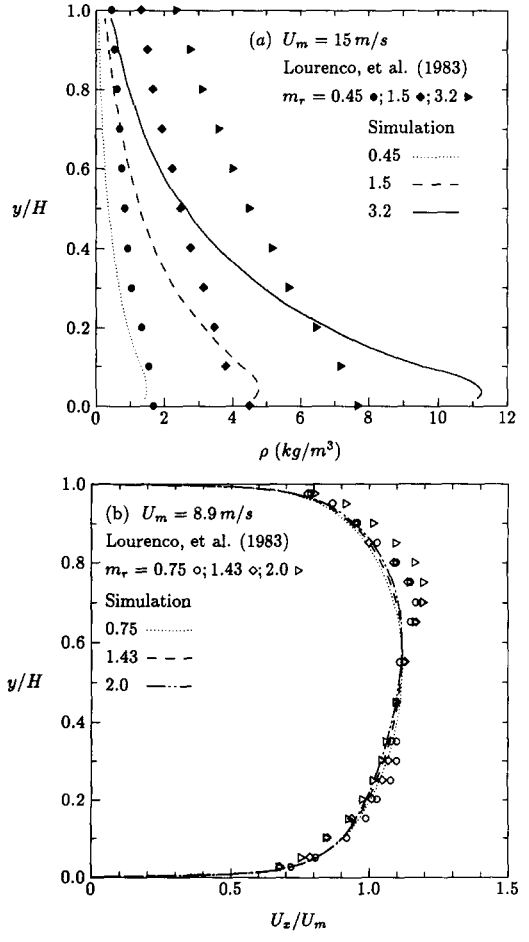

Figure 1. (a) Particle concentration and (b) mean air velocity (U_z/U_m).

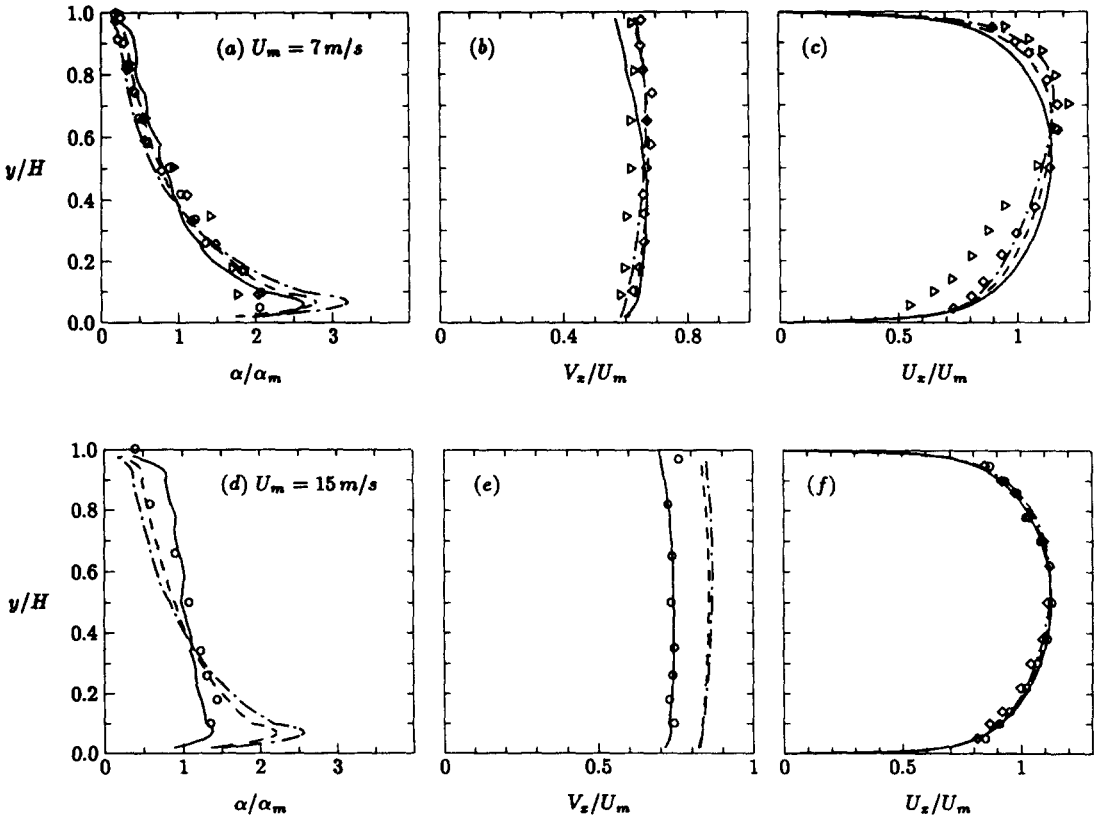

Figure 2. Particle concentration (α/α_m), mean particle velocity (V_s/U_m), and mean air velocity (U_s/U_m). Predictions: —, $m_r = 1$; – – –, $m_r = 3$; — · —, $m_r = 5$. Data of Tsuji *et al.* (1987) o, $m_r = 1$; ◇, $m_r = 3$; ▷, $m_r = 5$.

model (Launder and Spalding 1974) into the present dilute two-phase one seems reasonable; i.e. $C_\mu = 0.09$, $\sigma_k = 1.0$, $\sigma_\varepsilon = 1.3$, $C_{\varepsilon 1} = 1.44$ and $C_{\varepsilon 2} = 1.92$. The particles may still influence the distribution of the turbulence intensities *indirectly* through the interfacial couplings. In cases where the direct turbulence modulation is substantial, the question of how the closure coefficients might be affected is still an open one.

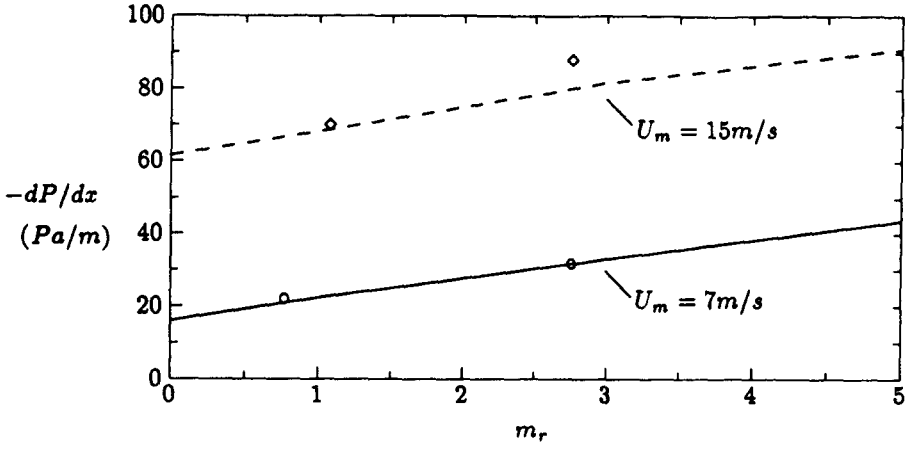

Figure 3. Variation of pressure gradient with loading ratio; predictions (curves) and measurements of Tsuji *et al.* (1987) (symbols).

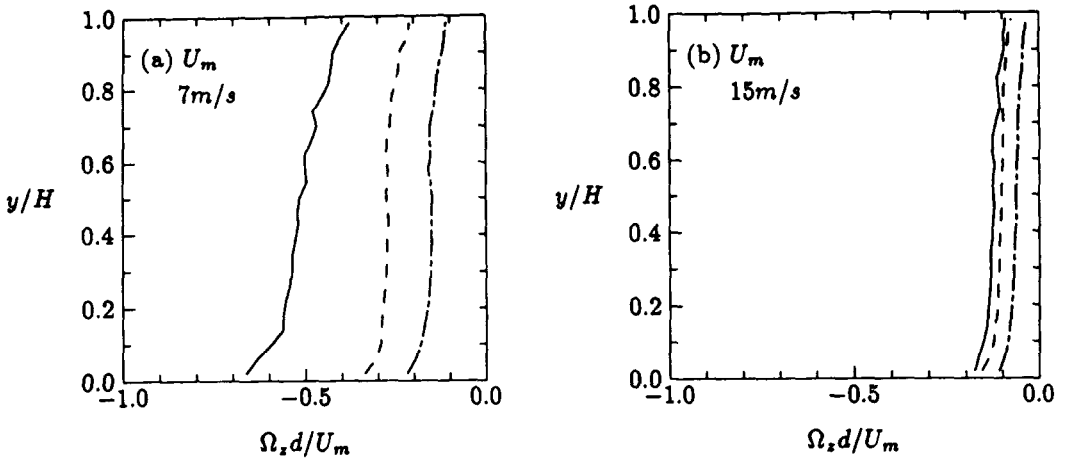

Figure 4. Mean particle angular velocity z-component. Simulations: —, $m_r = 1$; – – –, $m_r = 3$; – · –, $m_r = 5$.

Near the wall region, the eddy viscosity is written as

$$\mu_t = C_\mu f_\mu \rho_f \frac{k^2}{\epsilon}$$

where f_μ is a wall damping function given by

$$f_\mu = 1 - \exp(-y^+/5.2)$$

The dimensionless distance y^+ is expressed in wall unit defined as $y^+ = u_\tau y/\nu$ where $u_\tau = (\tau_w/\rho_f)^{0.5}$ is the friction velocity and τ_w is the shear stress at the wall.

3. EQUATIONS OF PARTICLE MOTION

The equation for translational motion of a particle in a turbulent fluid may be written as

$$m_p \frac{d\mathbf{v}}{dt} = m_p \mathbf{g} + \mathbf{F}_D + \mathbf{F}_{LS} + \mathbf{F}_{LM}. \quad [12]$$

The drag force is

$$\mathbf{F}_D = \frac{1}{8} \rho_f \pi d^2 C_D |\mathbf{v}_r| \mathbf{v}_r, \quad [13]$$

where the drag coefficient C_D is commonly given as (Clift and Gauvin 1971)

$$C_D = \frac{24}{Re_p} \quad (Re_p < 1)$$

$$C_D = \frac{24}{Re_p}(1 + 0.15 Re_p^{0.687}) \quad (1 < Re_p < 1000).$$

The Saffman (1965, 1968) lift due to fluid shearing motion is

$$\mathbf{F}_{LS} = 1.615(\rho_f \mu)^{1/2} d^2 C_{LS} \frac{dU_x}{dy}(u_x - v_x)\mathbf{e}_y \Big/ \left|\frac{dU_x}{dy}\right|^{1/2}. \quad [14]$$

According to Mei (1992), the coefficient C_{LS} may be expressed as

$$C_{LS} = (1 - 0.3314\gamma^{0.5})\exp(-0.1 Re_p) + 0.3314\gamma^{0.5} \quad (Re_p \leqslant 40)$$

$$C_{LS} = 0.0524(\gamma Re_p)^{0.5} \quad (Re_p > 40)$$

where $\gamma = |\mathrm{d}U_x/\mathrm{d}y|d/(2v_r)$. The Magnus lift due to particle rotation is

$$\mathbf{F}_{LM} = \frac{1}{2}\rho_f v_r^2 \frac{\pi d^2}{4} C_{LM} \frac{\boldsymbol{\omega}_r \times \mathbf{v}_r}{|\boldsymbol{\omega}_r||\mathbf{v}_r|}. \quad [15]$$

The Magnus lift coefficient C_{LM} may be written as (appendix A)

$$C_{LM} = \frac{d|\boldsymbol{\omega}_r|}{|\mathbf{v}_r|} \quad (\mathrm{Re}_p \leqslant 1)$$

$$C_{LM} = \frac{d|\boldsymbol{\omega}_r|}{|\mathbf{v}_r|}(0.178 + 0.822\mathrm{Re}_p^{-0.522}) \quad (1 < \mathrm{Re}_p < 1000).$$

In the above equations, m_p is the mass of a particle, U_x is the x-component of the mean fluid velocity, $\mathbf{u}$ and $\mathbf{v}$ are the instantaneous linear velocities of the fluid and the particle, respectively. The quantities $\mathbf{v}_r = \mathbf{u} - \mathbf{v}$ and $\boldsymbol{\omega}_r = \boldsymbol{\Omega}_f - \boldsymbol{\omega}$ are the instantaneous relative linear and angular velocities between the local fluid and the particle, respectively. The local mean angular velocity of the fluid is defined as $\boldsymbol{\Omega}_f = 0.5\nabla \times \mathbf{U}$.

Since the density ratio of gas to solid being considered in the present study is of the order 10^{-3}, the Basset force due to unsteady history effect and the virtual mass force due to acceleration of fluid surrounding the solid particle are small compared to the drag and the lifts. Thus they are neglected.

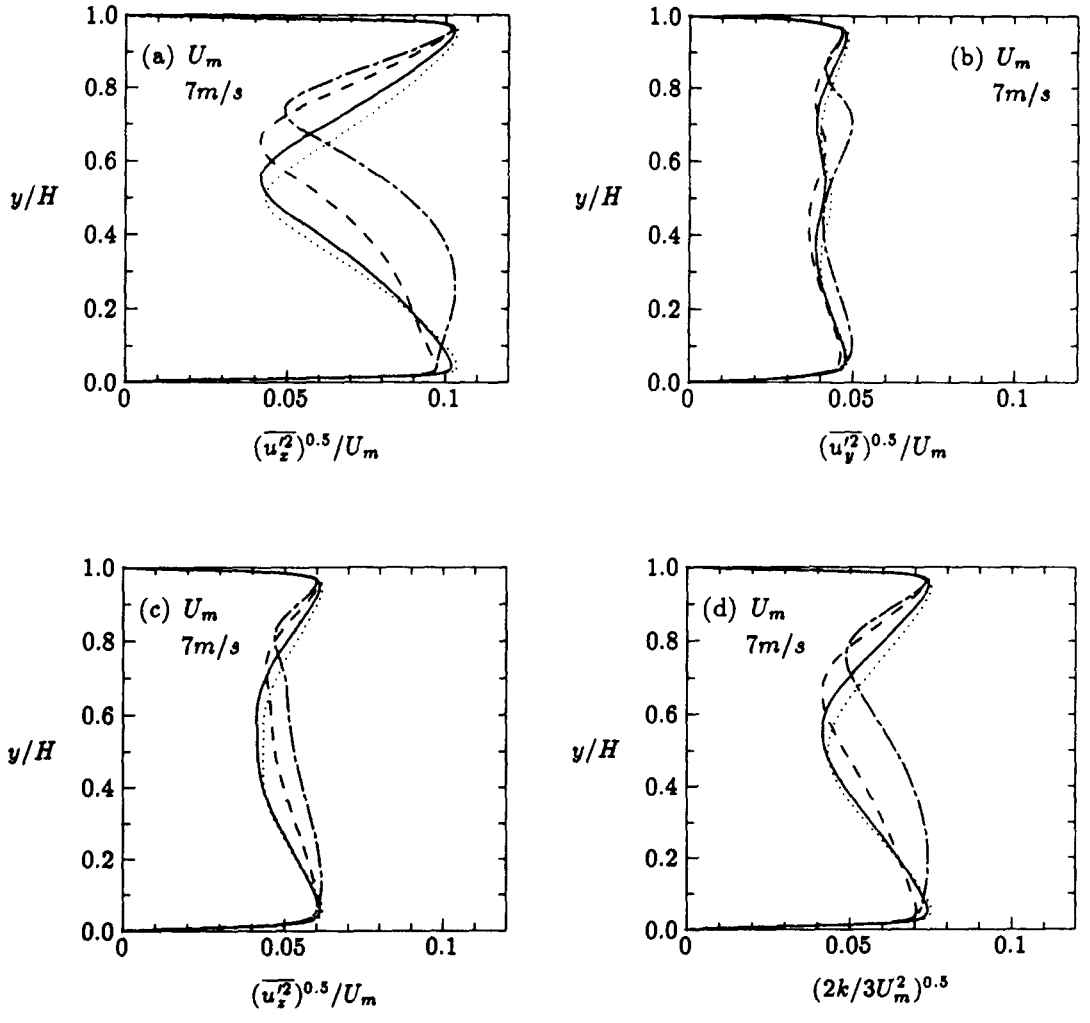

Fig. 5. (a)–(d)—(*caption facing page*)

The rate of angular momentum change of a spherical particle interacting with a viscous fluid may be written as (Dennis *et al.* 1980)

$$\frac{m_p d^2}{10}\frac{d\omega}{dt} = \frac{\rho_f d^2}{64}\left(\frac{6.45}{Re_\omega^{0.5}} + \frac{32.1}{Re_\omega}\right)|\omega_r|\omega_r \quad (20 \leqslant Re_\omega \leqslant 1000)$$

where the spin Reynolds number is defined as $Re_\omega = \rho_f d^2|\omega_r|/(4\,\mu)$.

4. COLLISION MODEL

The sticking–sliding collision model presented in Lun and Bent (1994) is employed for particle–particle collisions and particle–wall collisions in the present study. The model is simple and can produce result reasonably close to a number of experimental measurements.

Consider a collision between two inelastic, frictional spherical particles 1 and 2 with velocities $\mathbf{v}_1$ and $\mathbf{v}_2$, angular velocities $\boldsymbol{\omega}_1$ and $\boldsymbol{\omega}_2$, respectively. All collisions are regarded as binary and

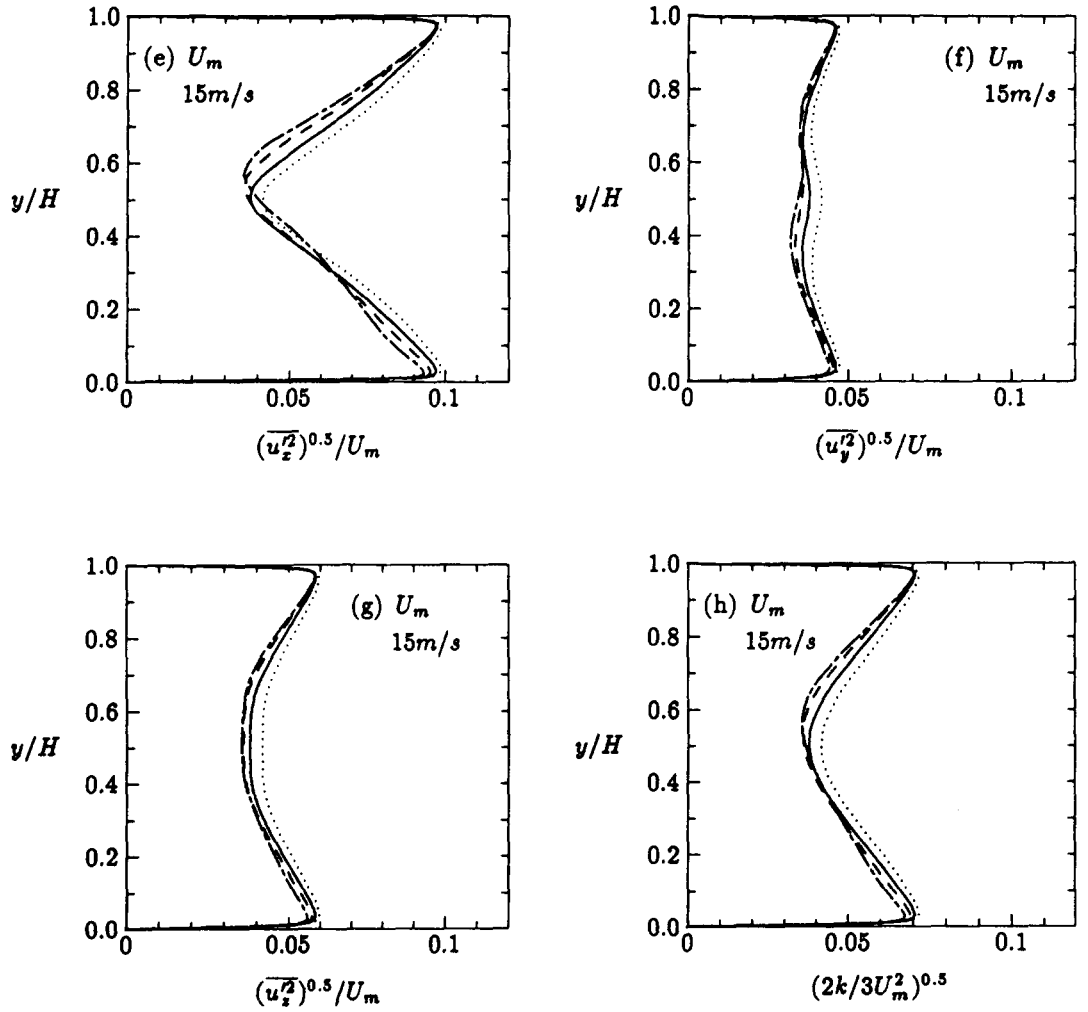

Fig. 5. (e)–(h)

Figure 5. Air turbulence intensities. Simulations: . . ., $m_r = 0$; —, $m_r = 1$; – – –, $m_r = 3$; – · –, $m_r = 5$.

instantaneous. During the impacts, the interstitial fluid effect is neglected. The peripheral velocities of particles 1 and 2 are

$$\mathbf{g}_1 = \mathbf{v}_1 - \frac{d}{2}(\mathbf{K} \times \boldsymbol{\omega}_1)$$

and

$$\mathbf{g}_2 = \mathbf{v}_2 - \frac{d}{2}(\mathbf{K} \times \boldsymbol{\omega}_2)$$

where $\mathbf{K}$ is the unit vector along the center line from particle 1 to particle 2. The total relative velocity, $\mathbf{g}_{12}$, at the contact point just prior to the collision is

$$\mathbf{g}_{12} = \mathbf{v}_{12} - \frac{d}{2}(\mathbf{K} \times \boldsymbol{\omega}_{12}) \quad [16]$$

where $\mathbf{v}_{12} = \mathbf{v}_1 - \mathbf{v}_2$ and $\boldsymbol{\omega}_{12} = \boldsymbol{\omega}_1 + \boldsymbol{\omega}_2$. The components of $\mathbf{g}_{12}$ are changed in a collision such that

$$\mathbf{K} \cdot \mathbf{g}_{12}^* = -e_p(\mathbf{K} \cdot \mathbf{g}_{12}), \quad [17]$$

$$\mathbf{K} \times \mathbf{g}_{12}^* = -\beta_p(\mathbf{K} \times \mathbf{g}_{12}) \quad [18]$$

where quantities with superscript asterisk denote post-collisional values, e_p is the coefficient of

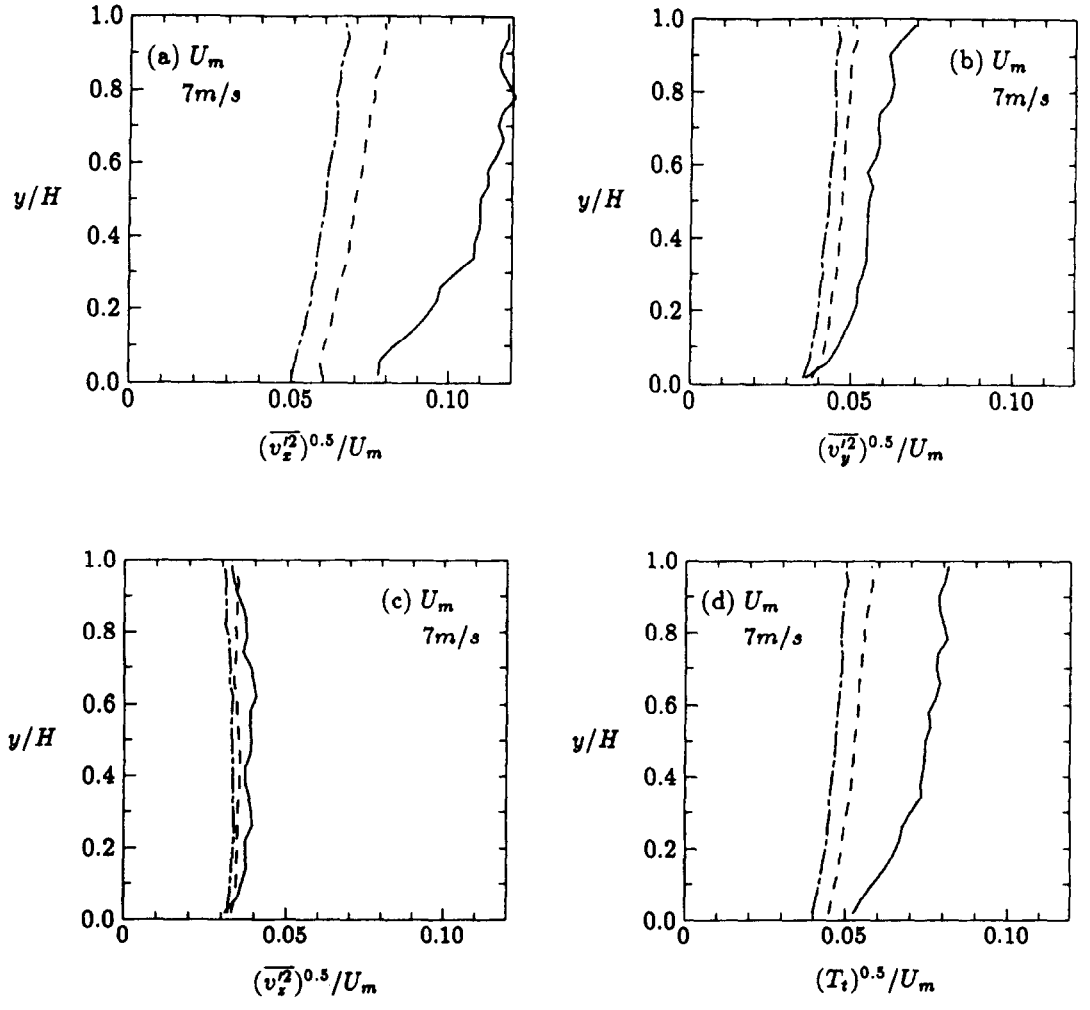

Fig. 6. (a)–(d)—(*caption facing page*)

restitution in the normal direction, and β_p is called the coefficient of restitution in the tangential direction at the point of contact.

Using [17] and [18] in [16] the relationships between the pre- and post-collisional velocities can be written as

$$m_p(\mathbf{v}_1 - \mathbf{v}_1^*) = m_p(\mathbf{v}_2^* - \mathbf{v}_2) = \mathbf{J}, \quad [19]$$

$$I(\omega_1^* - \omega_1) = I(\omega_2^* - \omega_2) = -d(\mathbf{K} \times \mathbf{J})/2, \quad [20]$$

and

$$\mathbf{J} = m_p\eta_2\mathbf{g}_{12} + m_p(\eta_1 - \eta_2)\mathbf{K}(\mathbf{K}\cdot\mathbf{g}_{12}) \quad [21]$$

where $\mathbf{J}$ is the impulse, $\eta_1 = (1 + e_p)/2$, $\eta_2 = 0.5(1 + \beta_p)K_r/(1 + K_r)$, and $K_r = 4I/(m_p d^2)$ is a non-dimensional moment of inertia parameter ($K_r = 2/5$ for sphere).

It is evident in a number of experimental and theoretical investigations (Foerster *et al.* 1994; Johnson 1985; Maw *et al.* 1976, 1981; Goldsmith 1960) that the coefficient of normal restitution, e_p, decreases with increasing normal impact velocity. The tangential restitution process is rather complex (Maw *et al.* 1976, 1981). There can be no slip, micro slip or complete slip in the contact zone of the colliding bodies. As a result, the coefficient of tangential restitution at the contact point,

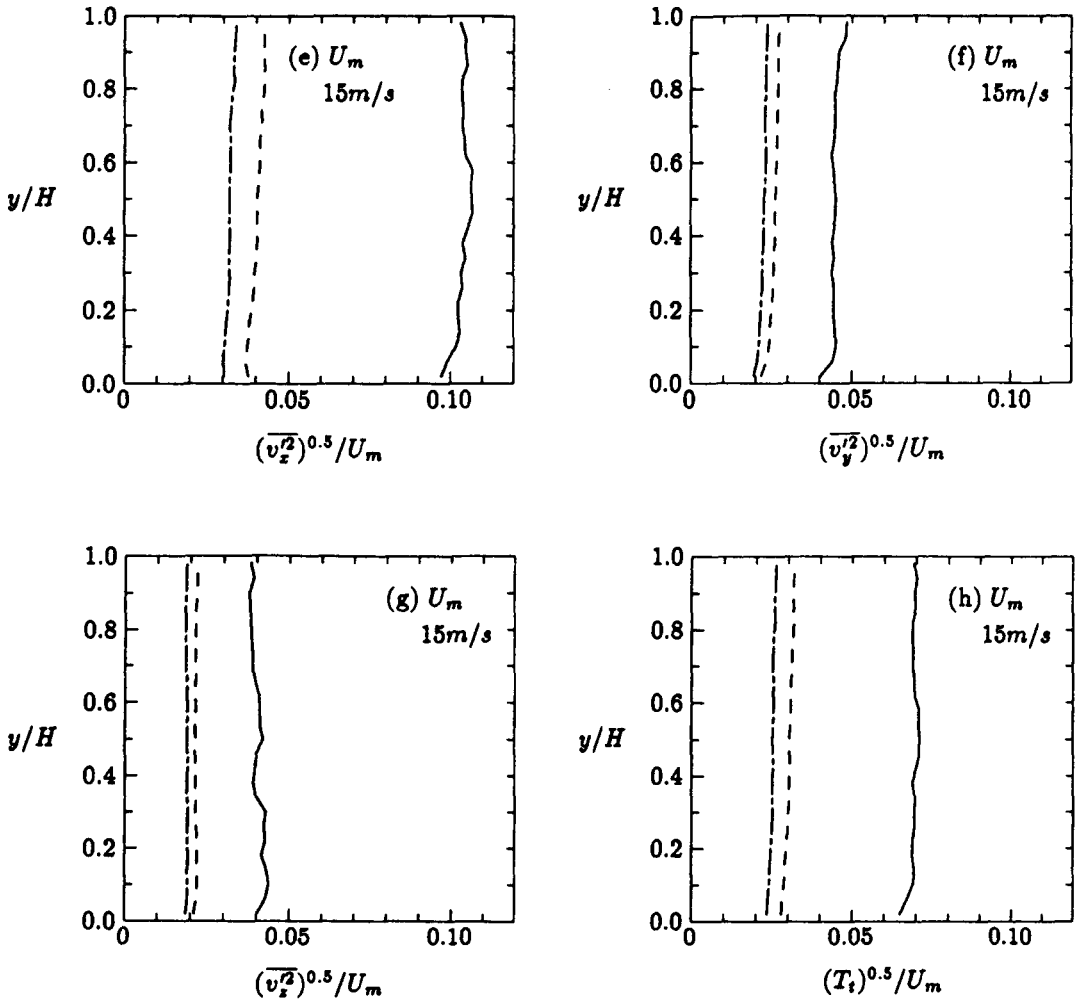

Fig. 6. (e)–(h)

Figure 6. Intensities of particle translational fluctuation velocity. Simulations: —, $m_r = 1$; – – –, $m_r = 3$; – · –, $m_r = 5$.

β_p, can be positive or negative and it depends on various parameters, for example friction, coefficient μ_p. A sticking–sliding model may be used to emulate the tangential restitution.

In oblique impacts, the normal and tangential impulses at the contact point are assumed to obey the Coulomb law of friction. In the case of tangential impulse being less than the product of the friction coefficient and the normal impulse, i.e. $|\mathbf{K} \times \mathbf{J}| < \mu_p|\mathbf{K}\cdot\mathbf{J}|$, *sticking contact* occurs. The surface tangential velocity is written as

$$\mathbf{K} \times \mathbf{g}_{12}^{*} = -\beta_0(\mathbf{K} \times \mathbf{g}_{12}), \qquad [22]$$

where β_0 is a constant characterizing the restitution of velocity in the tangential direction for sticking contacts, and in general, $0 \leqslant \beta_0 \leqslant 1$. Positive β_0 denotes particles rebounding with reverse spin caused by the restoration of elastic energy in the tangential direction.

On the other hand, when the tangential impulse is greater or equal to the product of the friction coefficient and the normal impulse, *sliding contact* occurs and the following equality applies,

$$|\mathbf{K} \times \mathbf{J}| = \mu_p|\mathbf{K}\cdot\mathbf{J}|. \qquad [23]$$

From [21] and [23], the tangential coefficient of restitution is found explicitly as

$$\beta_p = -1 + \mu_p(1 + e_p)(1 + K_r^{-1})|\mathbf{K}\cdot\mathbf{g}_{12}|/|\mathbf{K} \times \mathbf{g}_{12}|. \qquad [24]$$

When the collisional properties e_p, β_0 and μ_p, and the initial rotational and translational velocities

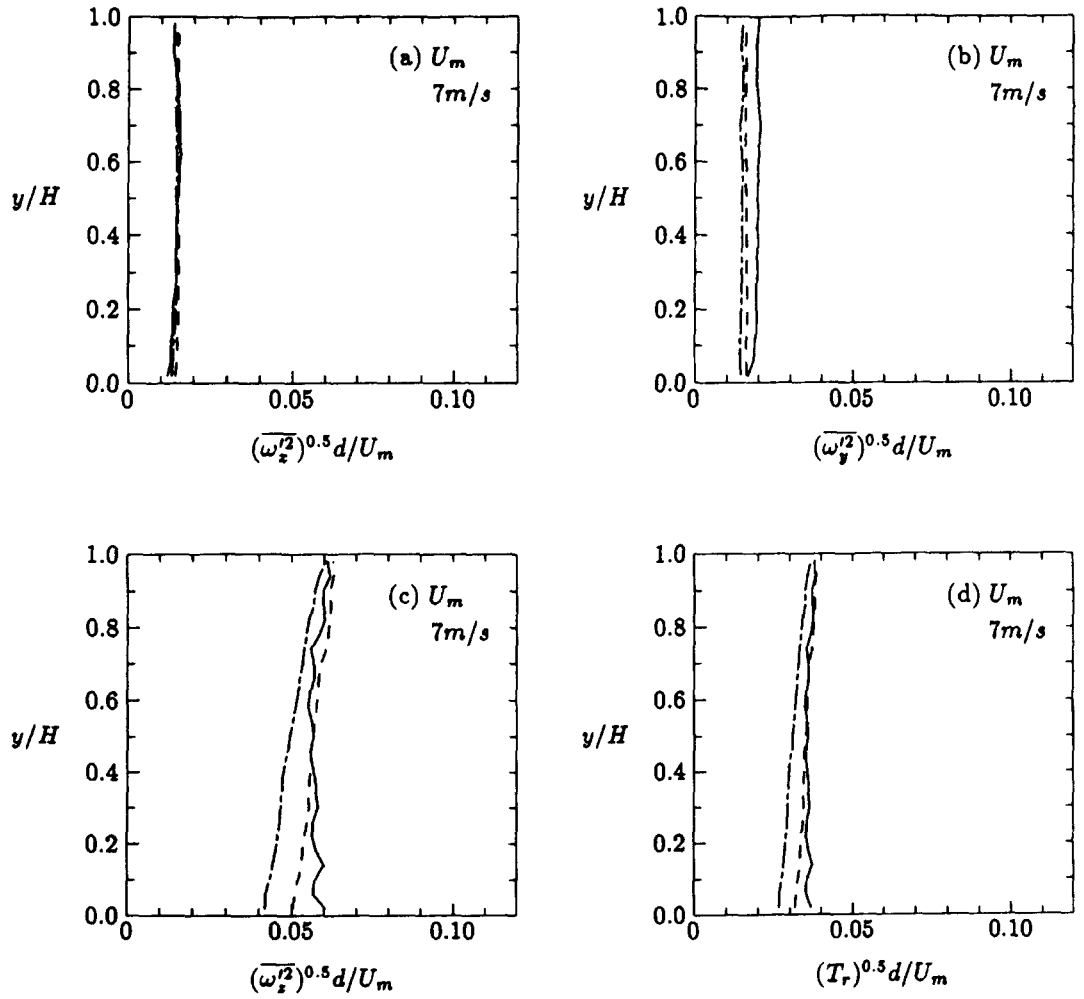

Fig. 7. (a)–(d)—(*caption facing page*)

of the particles are known, the impulse **J** in [21], the coefficient β_p in [22] or [24], and the post-collisional velocities in [19]–[20] can be determined.

In the case where a particle collides with a flat wall, the change in particle linear and angular momenta are

$$m_p(\mathbf{v}_1 - \mathbf{v}_1^*) = \mathbf{J}, \quad I(\boldsymbol{\omega}_1^* - \boldsymbol{\omega}_1) = -d(\mathbf{n} \times \mathbf{J})/2 \qquad [25]$$

and

$$\mathbf{J} = 2m_p\eta_2\mathbf{g}_{12} + 2m_p(\eta_1 - \eta_2)\mathbf{n}(\mathbf{n}\cdot\mathbf{g}_{12}), \qquad [26]$$

where **n** is the unit normal perpendicular to the flat wall surface.

Recently, Foerster *et al.* (1994) measured the coefficients e_p, β_0 and μ_p for collisions between small glass beads to be 0.97, 0.44 and 0.09, respectively. Inferring from the measurements of Maw *et al.* (1981), the mean coefficients e_p, β_0 and μ_p for steel pucks colliding with a steel block were 0.93, 0.40 and 0.123, respectively; similarly, for rubber pucks colliding with a rubber block, the coefficients were 0.86, 0.5, and 1.6, respectively.

5. NUMERICAL PROCEDURE

By using the above turbulent two-phase flow model, a computer program is developed to simulate a gas–solid suspension in a horizontal channel. Initially, a single-phase turbulent fluid flow

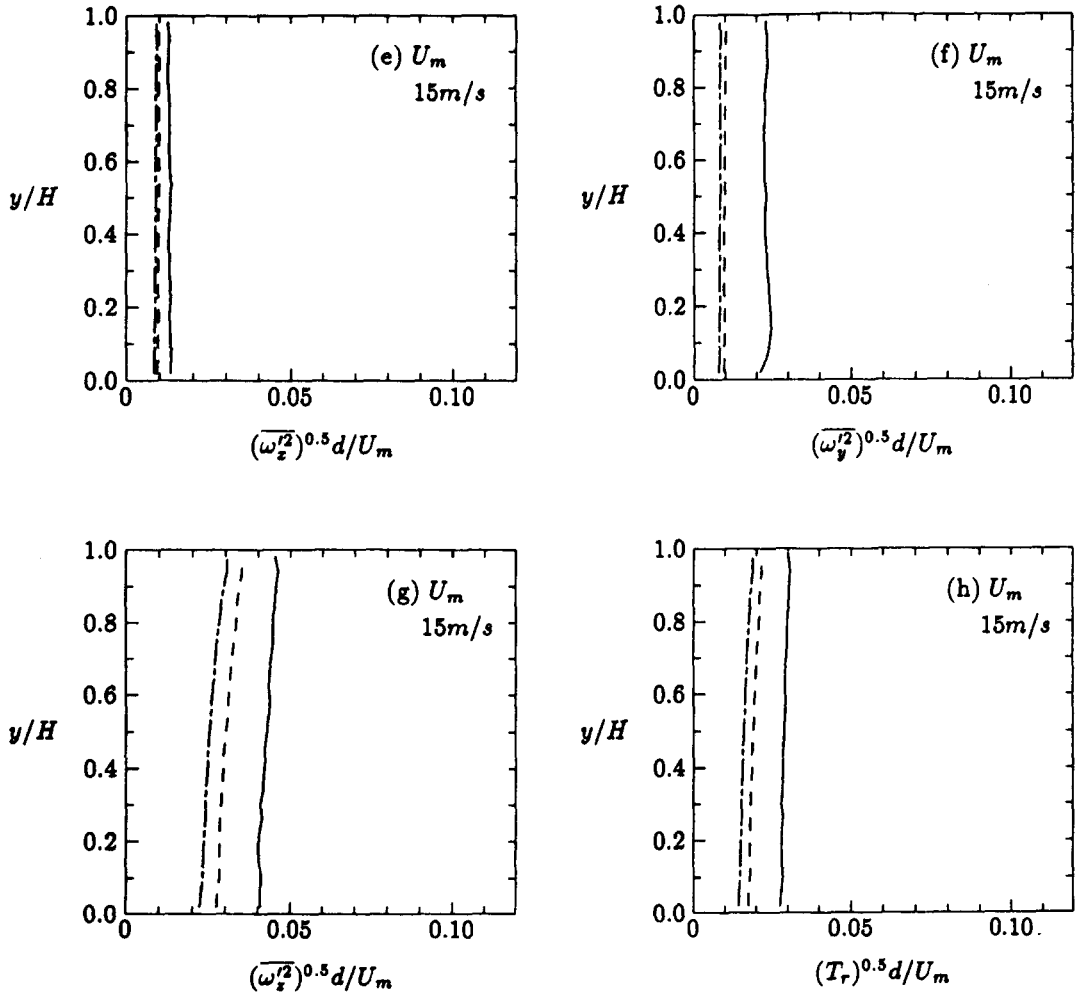

Fig. 7. (e)–(h)
Figure 7. Intensities of particle rotational fluctuation velocity. Simulations: —, $m_r = 1$; – – –, $m_r = 3$; – · –, $m_r = 5$.

field is computed for a specific bulk (or overall mean) fluid velocity $\mathbf{U}_m$ in a channel. The streamwise, the vertical and the spanwise directions are designated as the x-, y- and z-axes, respectively. The boundary conditions for the fully developed two-dimensional flow in a horizontal channel are

$$\frac{\partial U_x}{\partial x} = 0, \quad U_y = 0, \quad U_z = 0, \quad \frac{\partial p}{\partial x} = \text{const}, \quad \frac{\partial p}{\partial z} = 0, \quad \frac{\partial k}{\partial x} = 0, \quad \frac{\partial \epsilon}{\partial x} = 0.$$

On the solid walls, the boundary conditions for the mean fluid velocity and the turbulent kinetic energy are $U_x = 0$ and $k = 0$, respectively. The boundary condition for the rate of turbulent kinetic energy dissipation proposed by Hanjalic and Launder (1976) is used, i.e.

$$\epsilon = 2\nu\left(\frac{\mathrm{d}\sqrt{k}}{\mathrm{d}y}\right)^2.$$

The set of partial differential equations deduced from the conservation and constitutive equations in [5]–[11] are integrated numerically by the SIMPLE method (Patankar 1980) subject to the boundary conditions above. The Reynolds stress tensor in [7] reduces to the usual one

$$\left(\text{e.g. } \tau'_{xy} = -\rho_f \overline{u'_x u'_y} = \mu_t \frac{\partial U_x}{\partial y}\right)$$

while the turbulence intensities in [8] remain anisotropic. In order to verify the code, the computer program is used to simulate a number of experiments of single-phase turbulent gas flows in channels (Liu 1995). The numerical predictions for flow properties such as the mean fluid velocity and the anisotropic turbulence intensities are found to agree reasonably well with the experimental measurements.

Before one can integrate the equations of motion of the particles in [12], the distribution of the fluid phase properties must be known. The finite-difference (SIMPLE) method for the fluid phase can only provide mean quantities, while instantaneous properties are required in the particle equations of motion. The instantaneous fluid velocity is the sum of a mean component and a fluctuation component. The fluid fluctuation velocity at each node is sampled from a Gaussian distribution based upon the r.m.s. of the turbulence intensity in each direction. The mean and instantaneous fluid velocities at the particle center are linearly interpolated from values at the closest grid nodes of the fluid finite-difference scheme enclosing the particle.

In general, the fluid velocity probability density function can be skewed. Elghobashi and Truesdell (1993) found in their direct numerical simulation of low particle Reynolds number flows that the skewness of the grid-generated homogeneous turbulence decreases with increasing particle Reynolds number. They simulated flows in the range of $0 < \mathrm{Re}_p < 0.36$. In relatively high particle Reynolds number flows of the order 10^2, it is plausible that the skewness will become small and a normal distribution will suffice to approximate the real one.

Each fluctuation velocity represents an energetic eddy with a certain lifetime interacting with the solid particles in its vicinity. The eddy lifetime or sometimes called the interaction time is randomly sampled from a Gaussian distribution based upon the random lifetime of turbulent eddies with the Lagrangian integral timescale (Sommerfeld 1992). In the present study of dilute suspensions with large and massive particles moving at intermediate particle Reynolds number in the inertia regime, the direct turbulence modulation due to particle-induced turbulence is likely to be negligible and the mean Lagrangian integral timescale may be approximated by the correlation obtained in the single-phase fluid turbulent flows (Hinze 1975; Rizk and Elghobashi 1989)

$$T_L = 0.2\frac{k}{\epsilon}.$$

The fluid phase momentum equation in [6] contains a mean interfacial momentum flux per unit volume term, $\mathbf{M}$. From [4] and [12], the following expression is obtained

$$\mathbf{M} = \frac{\alpha\rho_p}{m_p n}\sum_{j=1}^{n}(\bar{\mathbf{F}}_{Dj} + \bar{\mathbf{F}}_{LSj} + \bar{\mathbf{F}}_{LMj}). \qquad [27]$$

The method of particle-source in cell was introduced by Crowe *et al.* (1977) to determine the momentum interaction term in [27]. Durst *et al.* (1984) and Tsuji *et al.* (1987) used similar methods in which **M** for a particular computational cell was equated to the sum of the net rate of momentum change (per unit volume) of particles passing through the cell.

The simulation program for the solid phase is mainly patterned after the work of Lun and Bent (1994). Depending on the mass loading ratio (mass flux ratio of solid phase to gas phase), solid particles are distributed randomly inside a control volume enclosed by the top and bottom solid flat walls and the four stationary periodic side walls. Initially, random fluctuation velocities in addition to a mean velocity close to $\mathbf{U}_m$ are assigned to each particle.

The motions of the particles are assumed to be uncorrelated and there is no other particle–particle interaction except direct hard collisions. This assumption is valid in dilute gas–solid flows. By numerically integrating the coupled translational and rotational equations of motion for each particle in a constant time step Δt (of the order 10^{-5} s), the particle can be advanced from one position to another. The particles are moved at very small time increment so that the particles are moved no more than 20% of the particle diameter each step. This ensures that the particles will not unknowingly pass through each other or the solid walls and the probability of simultaneous multiple collisions is eliminated. After all the particles had been moved, the distances between particle centers and between particles and solid walls are computed. For example, if the distance between two particle centers is less than a particle diameter, then a particle–particle collision had occurred within the last time step. Each collided particle is moved back to its old

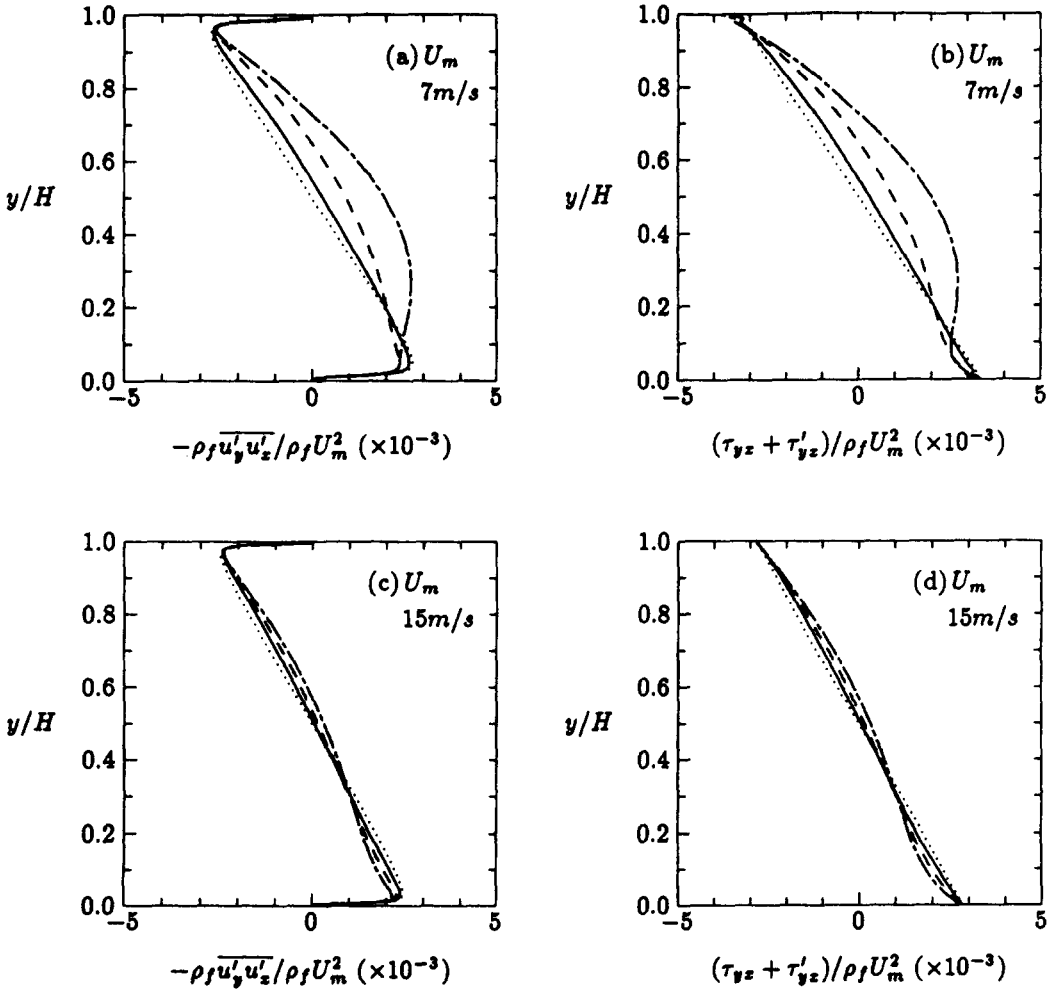

Figure 8. Reynolds shear stress ($-\rho_f\overline{u'_y u'_z}$) and total fluid shear stress ($\tau_{yz}+\tau'_{yx}$). Simulations: . . ., $m_r = 0$; —, $m_r = 1$; – – –, $m_r = 3$; – · –, $m_r = 5$.

position at Δt ago, and then to the location where it just touches its colliding partner. The impulse and the post-collisional particle velocities are calculated according to [19]–[21] or [25]–[26]. New trajectory for the collided particle is computed. If however no collision has occurred at all or after all the collisions have been dealt with, every particle is moved again for another Δt. After a specific time ($500\Delta t$, say), new fluid properties are computed by incorporating into the fluid finite-difference calculation the information obtained from the solid phase computation, namely the mean solid volume fraction and the mean interfacial momentum flux per unit volume associated with each grid cell. The new mean fluid properties will subsequently be used in the solid phase computation. Such a two-way coupling iterative procedure continues until a specific time for ending the computation is reached.

Large cumulative statistical samples (appendix B) are taken only after the flow has become steady and fully developed. The bulk particle velocity and the total kinetic energy of the solid phase are used as indicators for determining whether the flow has reached steady state or not. Typically, a steady flow is established after 1000 collisions per particle. For example, the simulation program running in a Microway Number Smasher-860-40 MHz coprocessor board takes about 48 h of real time to finish about 6000 collisions per particle for a suspension with 501 particles.

6. RESULTS

Figure 1 shows the comparison between the simulation result and the experimental measurements of the distributions of particle concentration and mean gas velocity in air–solid

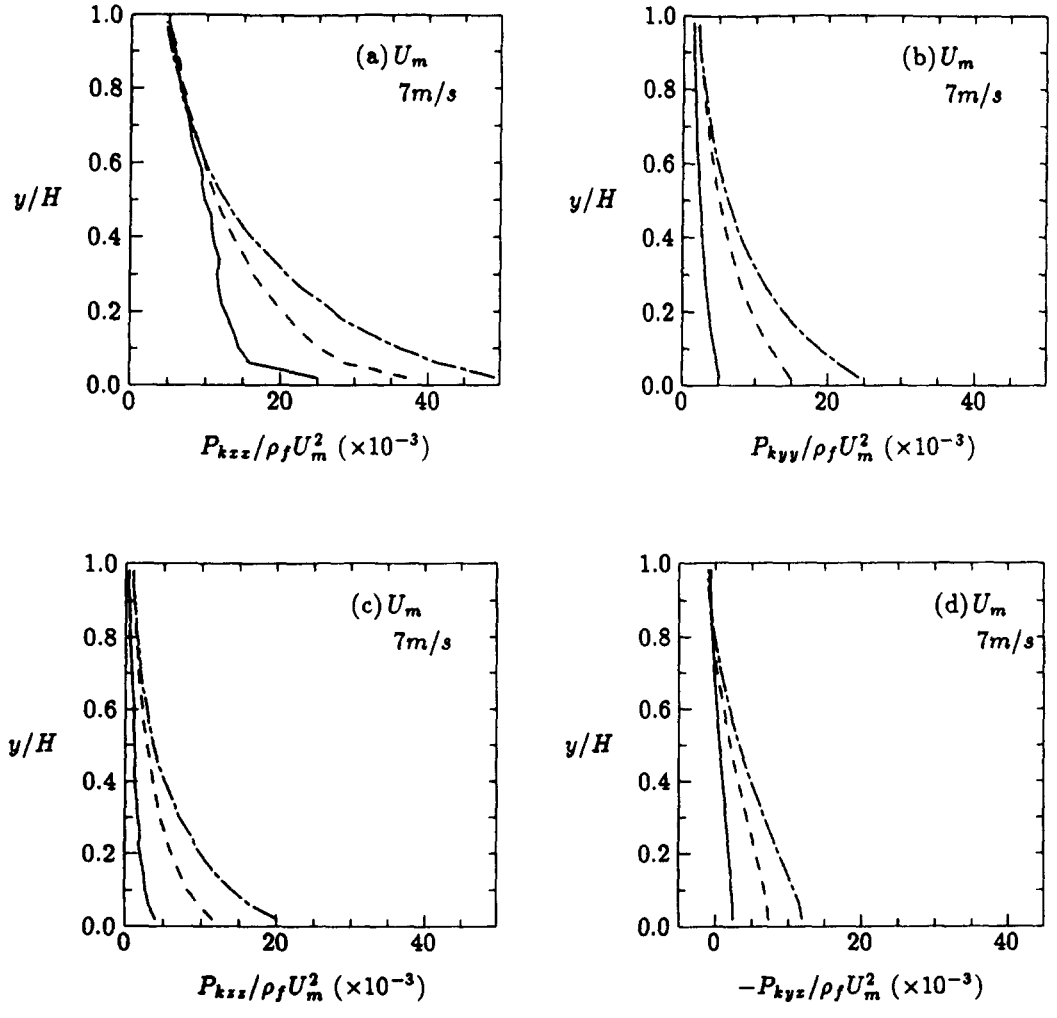

Fig. 9. (a)–(d)—(*caption facing page*)

two-phase flows in a horizontal channel (Lourenco *et al.* 1983). The channel height H was 50 mm. High velocity air (with mass density ρ_f of 1.2 kg/m^3 and dynamic viscosity μ of 1.8 $\times$ 10^{-5} Pas) was used to suspend and transport spherical glass beads along the channel. The diameter and the mass density of the glass beads were 0.5 mm and 2400 kg/m^3, respectively. The bulk air velocities tested in the experiments were U_m = 8.9 and 15 m/s, and the corresponding channel Reynolds numbers, $\mathrm{Re}_H = \rho_f U_m H/\mu$, were 29,667 and 50,000.

Detailed information about the channel and the materials tested is unfortunately not available. For simplicity, the collisional properties (e_p, β_0 and μ_p) for both the particle–particle collisions and the particle–wall collisions are assumed to be identical. In other words, the collisional properties are regarded as some mean quantities appropriate for the flow system. Foerster *et al.* (1994) measured the mean coefficients for normal restitution (e_p), tangential restitution at the contact point for sticking contacts (β_0), and friction (μ_p) to be 0.97, 0.44 and 0.09, respectively, for small *smooth* glass beads. The friction coefficient for the glass beads used by Lourenco *et al.* (1983) is unknown. However, glass is brittle. The numerous collisions that each particle suffered would have caused multiple microfractures at its surface and thus a friction coefficient higher than the initial value. The simulation result presented in figure 1 is based on a friction coefficient of 0.40.

Due to gravity, the particle concentration (ρ) increases from the top to the bottom of the channel as shown in figure 1(a). Evidently, it was difficult to control the loading and to measure the solids concentration distribution in such type of experiments. There were significant discrepancies between the *bulk* solids concentration (ρ_m) (or equivalently the mass loading ratio, m_r) reported

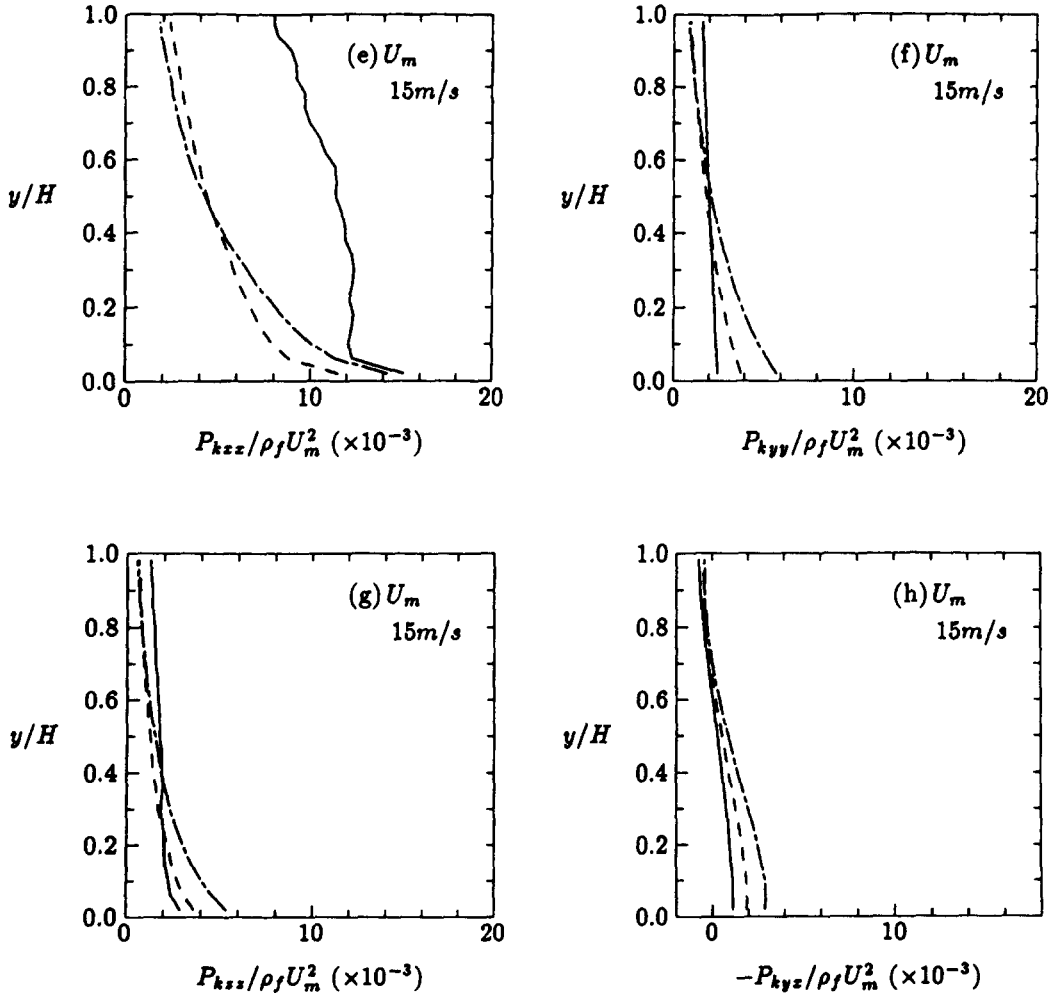

Fig. 9. (e)–(h)
Figure 9. Particle kinetic stresses. Simulations: —, m_r = 1; – – –, m_r = 3; – · –, m_r = 5.

by Lourenco *et al.* (1983) and the values actually obtained from the measured distributions. From the test data (figure 1(a)), one may estimate ρ_m for each profile by dividing the sum of the concentration readings across the flow field by the number of data points. The values for ρ_m are found to be 0.95, 2.62 and 4.77 kg/m^3 corresponding to the profiles with m_r of 0.45, 1.5 and 3.2 respectively, whereas the values for ρ_m given by the products of m_r and the air density are 0.54, 1.8 and 3.84 kg/m^3. The difference between the two sets of ρ_m ranges between 24 and 76%. In other words, the actual mass loading in the flows should have been about 0.79, 2.19 and 4.0 instead of 0.45, 1.5 and 3.2.

The mean air velocity profile predicted by the present simulation agree qualitatively with the experimental measurements for $U_m = 8.9$ m/s and m_r of 0.75, 1.43 and 2.0 as shown in figure 1(b). Lourenco and Essers (1983) pointed out that the intrusion of the air velocity probe into the flow field induced certain additional perturbation in the measurements. Nonetheless, it is evident in both the predictions and the measurements that the asymmetry of the mean air velocity profile becomes more and more pronounced as the loading ratio increases. For single-phase turbulent air flow at high Reynolds number, the fluid velocity profile is essentially symmetric across the channel height. Due to gravity, the particle concentration is higher near the bottom than elsewhere. The relatively higher solids concentration near the bottom causes higher resistance to the air motion than those in the upper region. As a result, the air moves relatively slower near the bottom than near the top. It is noteworthy that m_r of 0.75, 1.43 and 2.0 correspond to bulk solids volume fraction (α_m) of 3.75×10^{-4}, 7.15×10^{-4} and 0.001, respectively. Thus, even in these very dilute systems, the

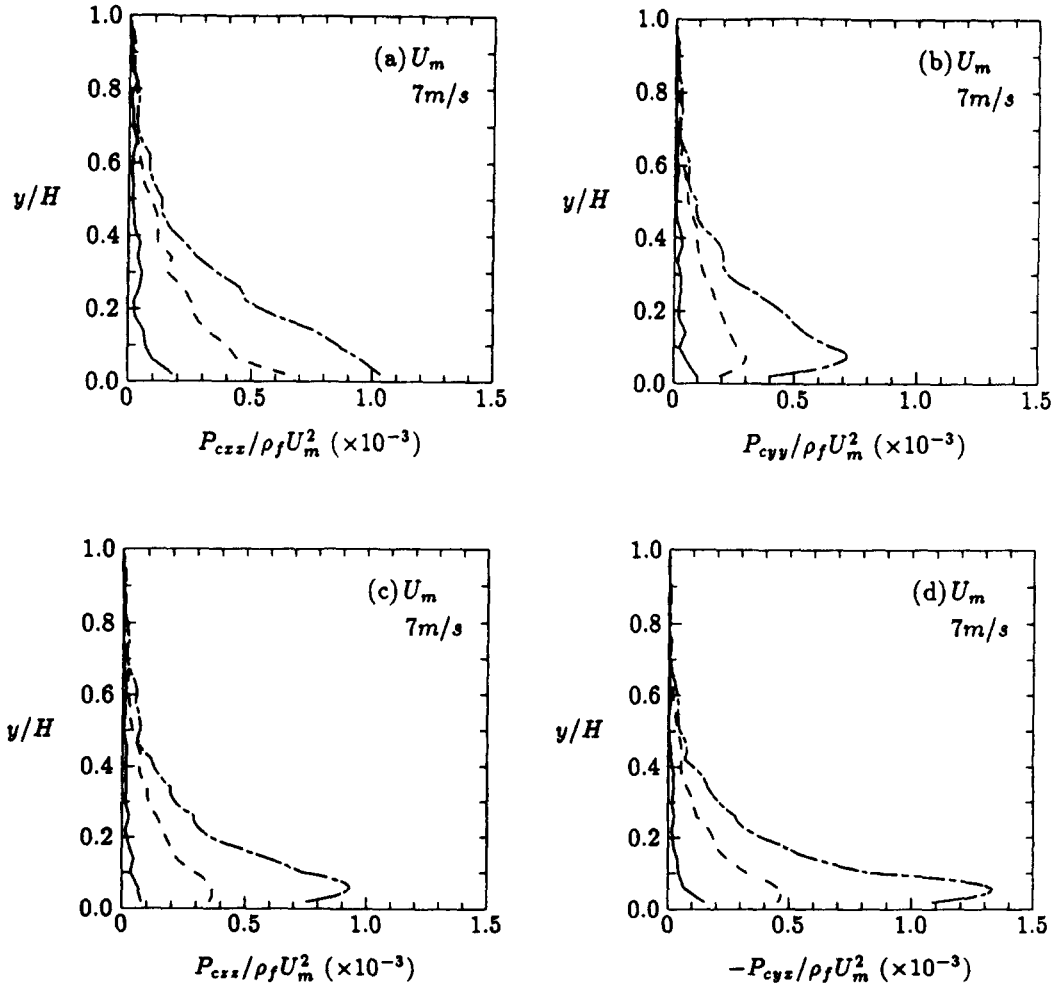

Fig. 10. (a)–(d)—(*caption facing page*)

interfacial coupling effect which is responsible for the asymmetry of the mean fluid velocity profile may not be neglected.

Next, the computer program is applied to simulate the turbulent air-solid flows in the horizontal channel experiment of Tsuji *et al.* (1987). The channel height H was 25 mm. The bulk air velocities tested in the experiments were $U_m = 7$ and 15 m/s which yielded the channel Reynolds numbers (Re_H) of 11,667 and 25,000, respectively. The solid phase was composed of polystyrene beads with 1 mm diameter and mass density of 1000 kg/m^3. The particle-wall friction coefficient was 0.4. The mass loading ratio, m_r, were 1, 3 and 5 which corresponded to α_m of 0.0012, 0.0036 and 0.006, respectively. Tsuji *et al.* used a pitot tube to measure the air velocity, and a fiber optic probe to measure the particle velocity and number density.

Tsuji *et al.* (1987) suggested an e_p of 0.8 for the polystyrene beads colliding with the solid walls. Unfortunately, there is no information about the coefficients for normal restitution and tangential restitution for the particle–particle collisions. Again for simplicity, the particle–particle collisional properties (e_p, β_0 and μ_p) are taken to be identical to those for particle–wall collisions and they are regarded as some average values suitable for the flow system. The values of $e_p = 0.9$, $\beta_0 = 0.4$ and $\mu_p = 0.47$ are used in the computations, unless specified otherwise.

The normalized solids volume fraction distribution predicted by the simulation is compared with the experimental measurements of Tsuji *et al.* (1987) in figure 2(a) and (d). Fair agreement is found among the two. The predicted profiles show that a maximum solids concentration is located at a

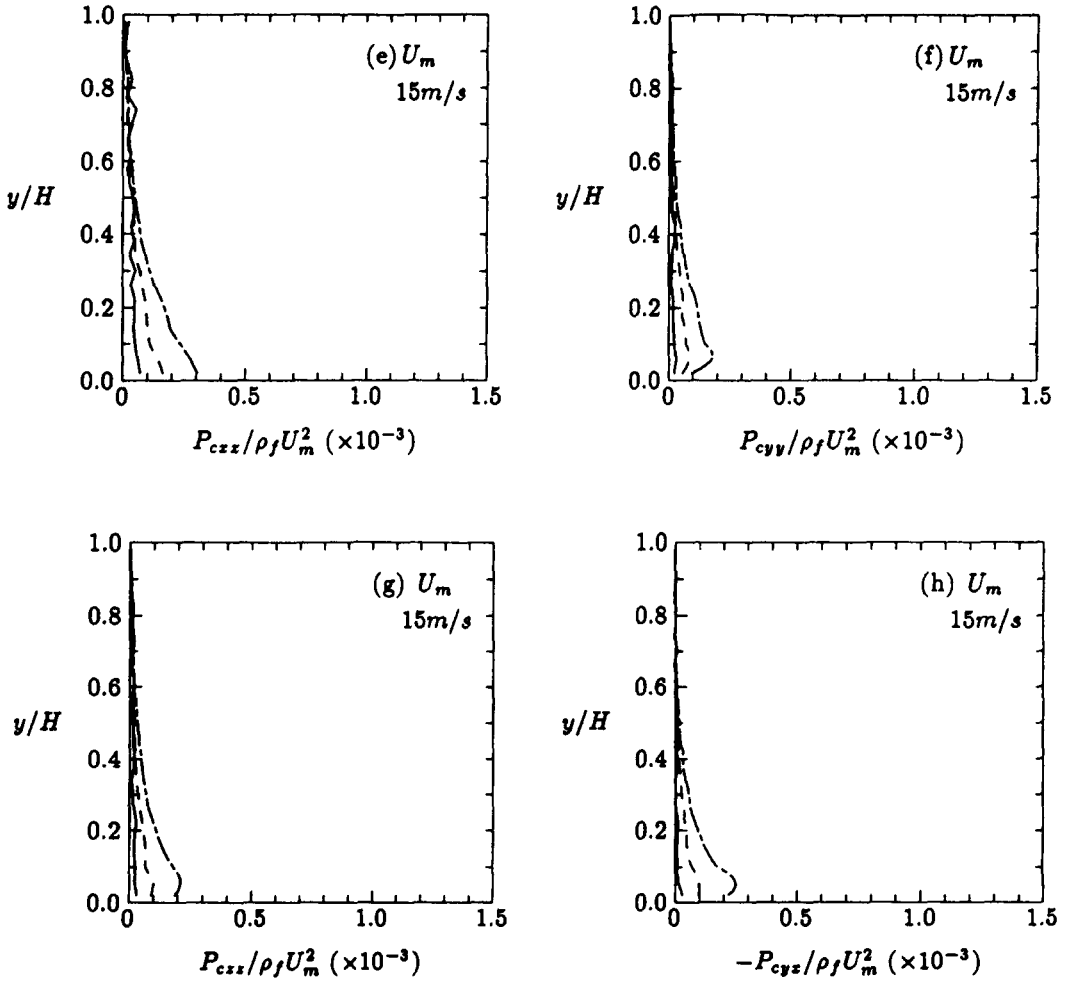

Fig. 10 (e)–(h)
Figure 10. Particle collisional stresses. Simulations: —, $m_r = 1$; – – –, $m_r = 3$; – · –, $m_r = 5$.

small distance away from the bottom wall. Similar behavior was reported in the numerical studies of Tsuji *et al.* (1987) and Oesterle and Petitjean (1993).

When the present computer program is set to treat *only* particle–wall collisions and ignore any interparticle ones, all the solid particles are found to deposit and roll along the bottom of the channel similar to what Tsuji *et al.* (1987) had found. Changing the collisional properties of the particles would either quicken or prolong the deposition process. However, when particle–particle collisions are incorporated in the computations a steady and fully developed suspension is resulted. There is no need of any virtual wall model because energy and momentum can be transferred through the solid phase by means of interparticle collisions. It is noteworthy that the percentages of the number of interparticle collisions to the total number of collisions are 10, 48 and 66 for $U_m = 7$ m/s corresponding to α_m of 0.0012, 0.0036 and 0.006, respectively; similarly, the percentages are 26, 52 and 67 for $U_m = 15$ m/s. The percentages of the number of interparticle collisions turned out to be quite high in these dilute systems. One major implication is that the effect of interparticle collisions is one of the dominant contributors in sustaining the solid phase in a full suspension, and its effect should not be neglected even in dilute systems such as the ones studied here.

The numerical results and the experimental measurements for the dimensionless mean particle velocity distribution (V_x/U_m) are in good agreement as shown in figure 2(b) and (e). The predicted profiles are in general asymmetric due to gravity and interfacial coupling effects. For the range of mass loading simulated, the mean particle Reynolds number is found to range approximately between 10 to 380 for bulk velocities of $U_m = 7$ and 15 m/s.

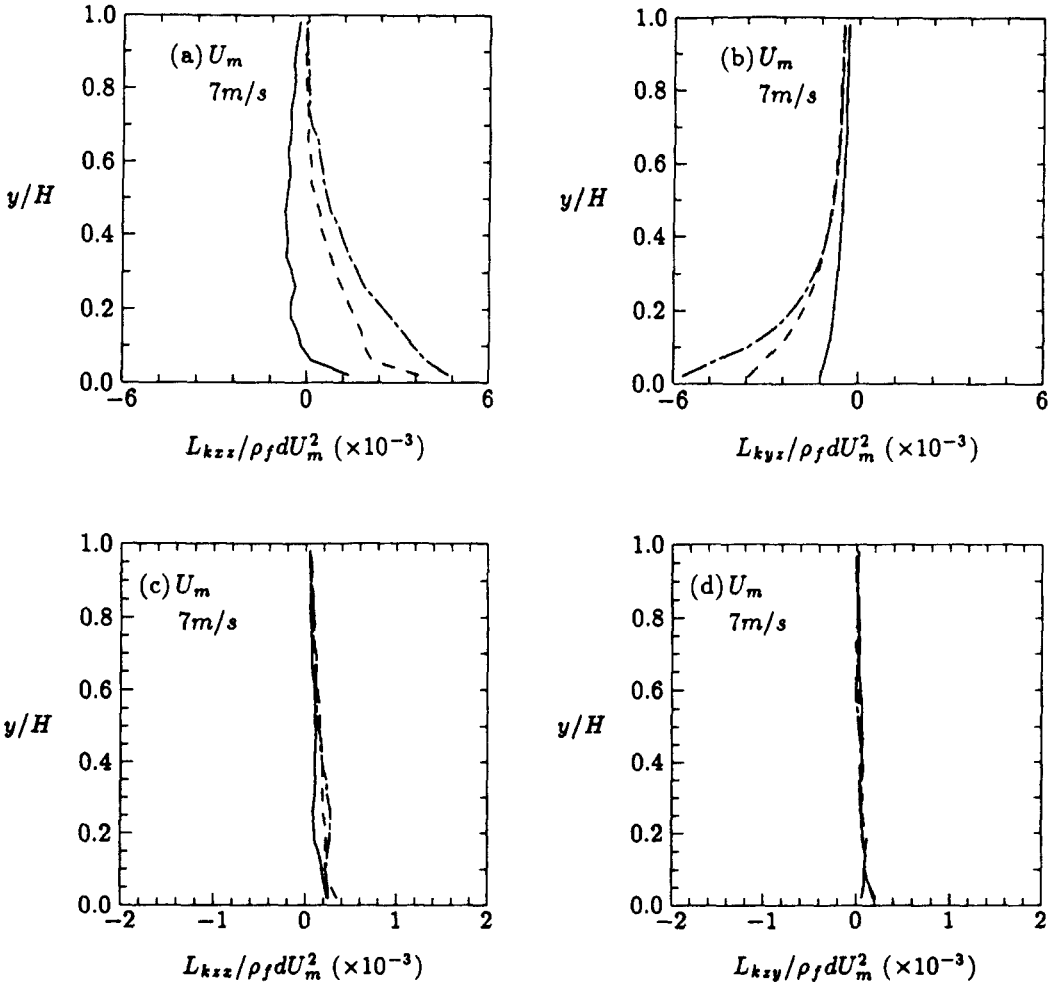

Fig. 11. (a)–(d)—(*caption facing page*)

In figure 2(c) and (f), there is reasonable agreement between the predictions and the experimental measurements for the mean air velocity distribution. The results are similar to those observed earlier in the test data of Lourenco *et al.* (1983) in figure 1(b). The mean air velocity distribution becomes increasingly asymmetric with the increase of mass loading.

When the fluctuation component of the fluid velocity is set to be zero, in other words the turbulent forcing was turned off in the solid phase simulation, the mean flow properties (such as solids concentration, gas and particle velocities) show no appreciable changes in their distributions. Typically the mean particle velocity is reduced by about 2%. This result is consistent with our assumption that the fluctuations of both fluid and particle properties are uncorrelated. Louge *et al.* (1991) studied dilute two-phase flow systems with particles massive enough to be unaffected by the velocity fluctuations in the turbulent gas. They 'extended' Koch's correlation (Koch 1990) between the velocity fluctuations of the gas and those of the particles for Stokes flows ($u_i' v_i'$) to the Newtons flows by employing a modified relaxation time. They commented that the contribution of $u_i' v_i'$ is typically dominated by other terms.

Pressure drop in pneumatic-transport devices is an important design parameter. Good agreement is found between the predictions and the measurements of Tsuji *et al.* (1987) for the variation of the pressure gradient with the loading ratio as shown in figure 3. As one might expect, the pressure drop which is caused by the losses in both the solid phase and the gas increases with increasing mass loading.

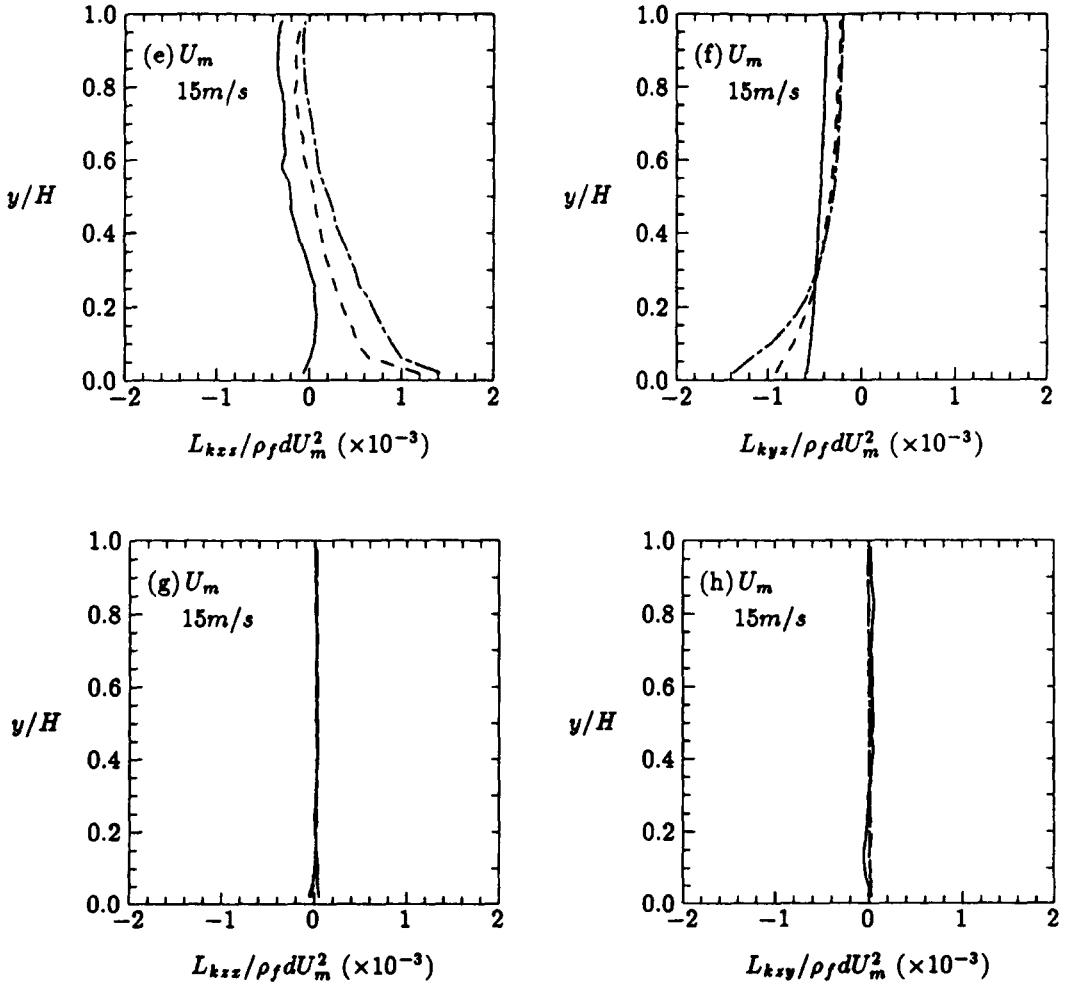

Fig. 11. (e)–(h)

Figure 11. Particle kinetic angular momentum fluxes. Simulations: —, $m_r = 1$; – – –, $m_r = 3$; – · –, $m_r = 5$.

Figure 4 shows the distribution of the z-component of mean dimensionless particle angular velocity ($\Omega_z d/U_m$). Particle rotations are induced by a number of factors such as frictional collisions between the particles themselves or between the particles and the solid-walls. The negative mean angular velocity in the z-direction indicates that on average the particles rotate in the clockwise manner. The x- and y-components of $\boldsymbol{\Omega}$ are negligibly small. The relative angular velocity between a particle and the fluid in the clockwise direction produces a Magnus lift in the vertically upward direction which helps suspending the particle against gravity. Furthermore, the mean particle spin velocity increases with decreasing loading ratio. Such an increase actually compensates to a certain degree for the diminishing support in maintaining a steady suspension through interparticle collisions since the number of interparticle collisions decreases with decreasing loading ratio. The mean particle spin Reynolds number ranges from about 30 to 340 for all the cases simulated here.

The variation of turbulence intensities with mass loading is shown in figure 5 for $U_m = 7$ and 15 m/s. The dotted curve represents the case of single-phase air flow. With the presence of relatively large solid particles, the air turbulence intensities are modified indirectly by the interfacial couplings in such a way that there can be turbulence enhancement in one region and attenuation in another. Unfortunately, Tsuji *et al.* (1987) did not measure the air turbulence intensities in their channel experiment. Previously, Tsuji and Morikawa (1982) measured the streamwise turbulence intensities of air–solid flows in a horizontal *pipe*. They found that in general the presence of relatively large plastic particles with 3.4 mm diameter increases the turbulence markedly, while small plastic

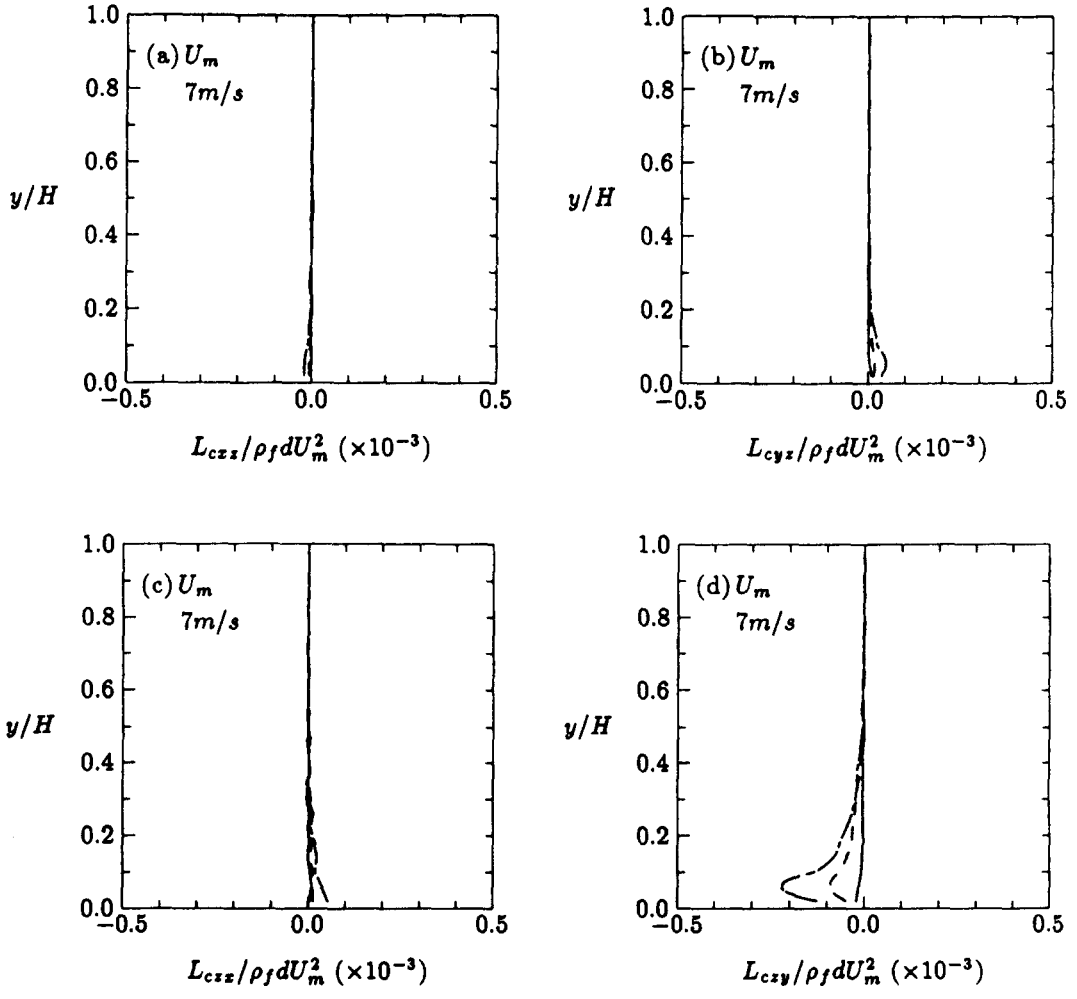

Fig. 12. (a)–(d)—(*caption facing page*)

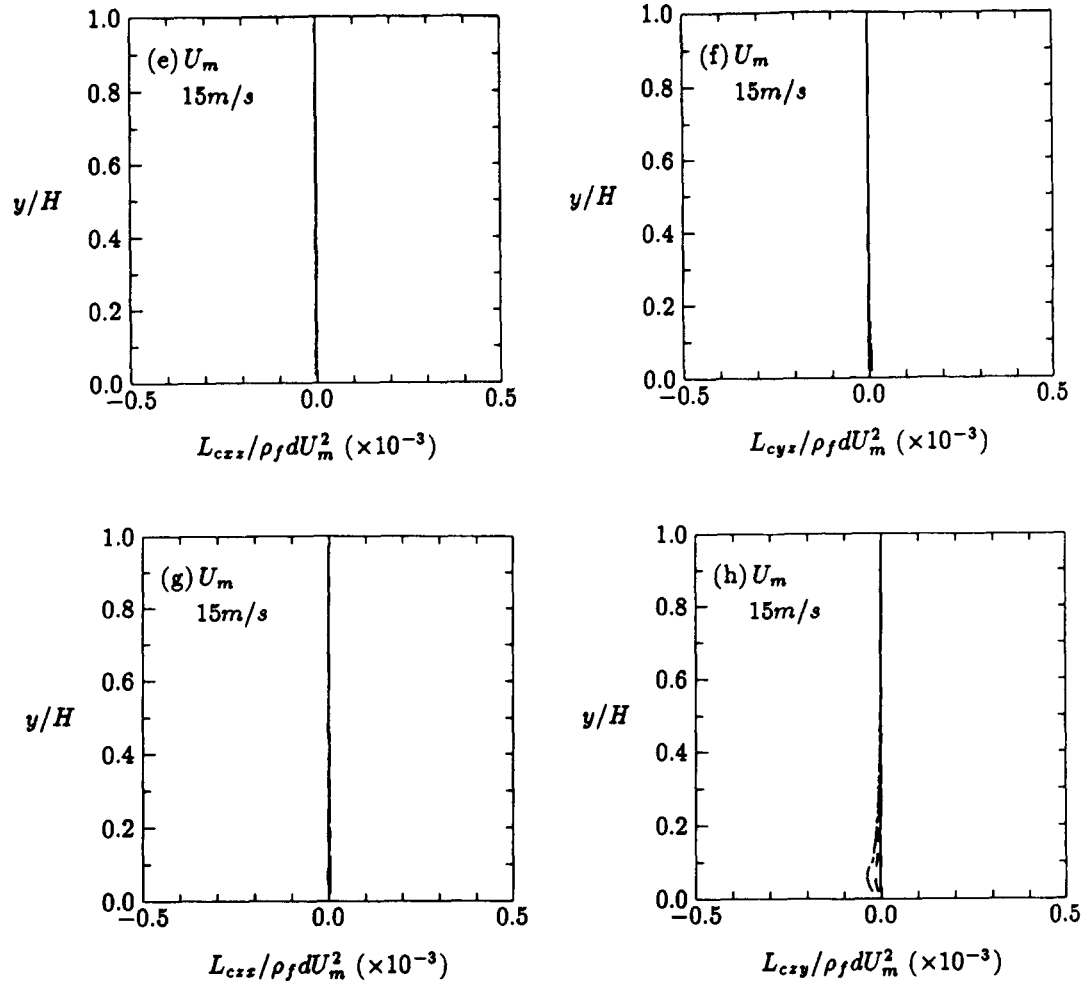

Fig. 12. (e)–(h)

Figure 12. Particle collisional angular momentum fluxes. Simulations: —, $m_r = 1$; – – –, $m_r = 3$; – · –, $m_r = 5$.

particles with 0.2 mm diameter reduced it. The present numerical model simulates particles with 1 mm diameter. Even though Tsuji and Morikawa used different materials and test conditions, one can still infer reasonable qualitative agreement between their measurements and the present predictions for the streamwise fluid turbulence intensities.

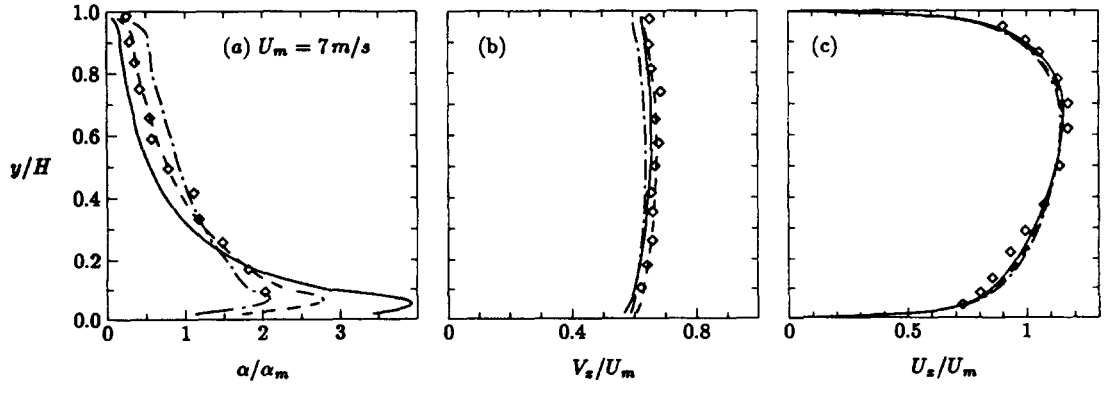

Figure 13. Particle concentration (α/α_m), mean particle velocity (V_z/U_m), and mean air velocity (U_z/U_m). Predictions for $m_r = 3$: —, $e = 0.8$; – – –, $e = 0.9$; – · –, $e = 0.95$. Data of Tsuji *et al.* (1987): ◇, $m_r = 3$.

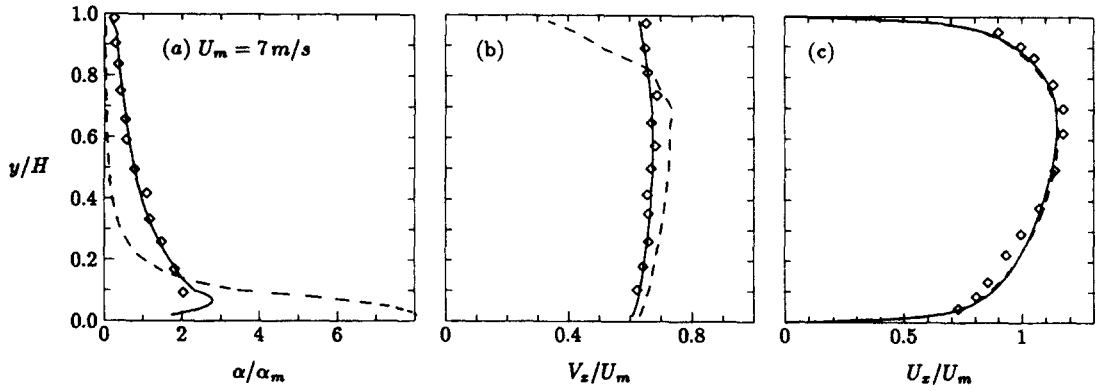

Figure 14. Particle concentration (α/α_m), mean particle velocity (V_x/U_m), and mean air velocity (U_x/U_m). Predictions for $m_r = 3$: —, $\mu_p = 0.47$; – – –, $\mu_p = 0.2$. Data of Tsuji *et al.* (1987): ◇, $m_r = 3$.

The effect of loading ratio on the intensities of particle translational fluctuation velocity (or the square root of the translational granular temperatures) is shown in figure 6. Comparing the intensity profiles in figures 5 and 6, one can observe that the magnitude of the translational fluctuation velocity intensities of the solid phase is comparable to their counterparts in the gas phase. The granular temperature decreases with increasing mass loading, and is somewhat higher in the upper region than in the lower one. Tsuji and Morikawa (1982) obtained similar behavior in the streamwise intensity of particle translational fluctuation velocity ($\sqrt{v_x'^2}$) as measured in their two-phase flow experiment with air and 0.2 mm plastic-beads in a horizontal pipe.

The intensities of particle rotational fluctuation velocities (or the square root of the rotational granular temperatures) are shown in figure 7. Similar to the turbulence intensities (figure 5) and the translational granular temperatures (figure 6), the rotational granular temperature is also anisotropic. The dominant component of the rotational granular temperature is in the z-direction.

The stress distributions of the gas phase and the solid phase are some very useful and interesting information which can be obtained readily in the simulation. In particular, the particle stress distributions are extremely difficult to measure in physical experiments and so far there has been no report of such quantities yet in two-phase flows.

Figure 8 shows the variation of the Reynolds shear stress and the total fluid shear stress with the mass loading and the bulk fluid velocity. As one may observe in the figure, the modification of the Reynolds (or the total) shear stress due to the presence of the particles is rather complex. Depending on the loading ratio and the bulk fluid velocity, there can be reduction, augmentation or a combination of both in fluid stresses across the channel height.

Figures 9 and 10 show the distributions of the particle kinetic stresses and the particle collisional stresses respectively. The particle normal stresses are clearly anisotropic. According to the kinetic theories of granular flow (Lun 1991; Lun and Savage 1987; Lun *et al.* 1984), the particle kinetic

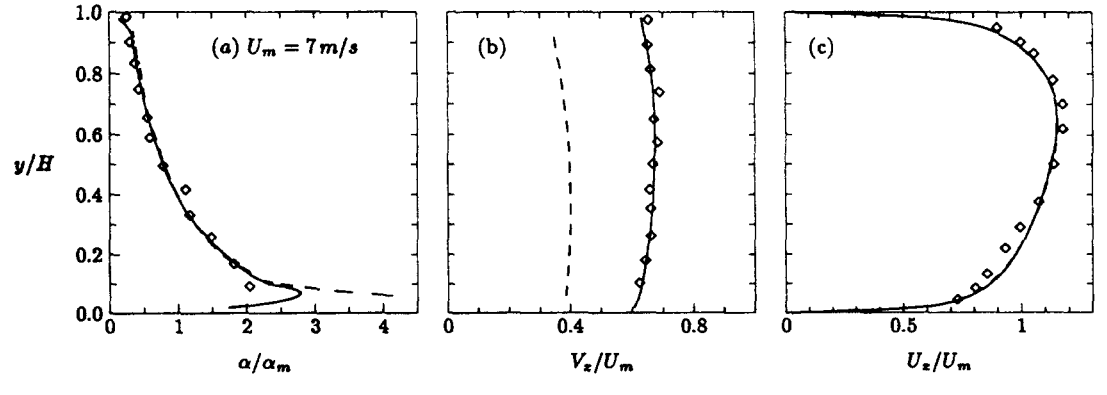

Figure 15. Particle concentration (α/α_m), mean particle velocity (V_x/U_m), and mean air velocity (U_x/U_m). Predictions for $m_r = 3$: —, $d = 1$ mm; – – –, $d = 2$ mm. Data of Tsuji *et al.* (1987): ◇, $m_r = 3$, $d = 1$ mm.

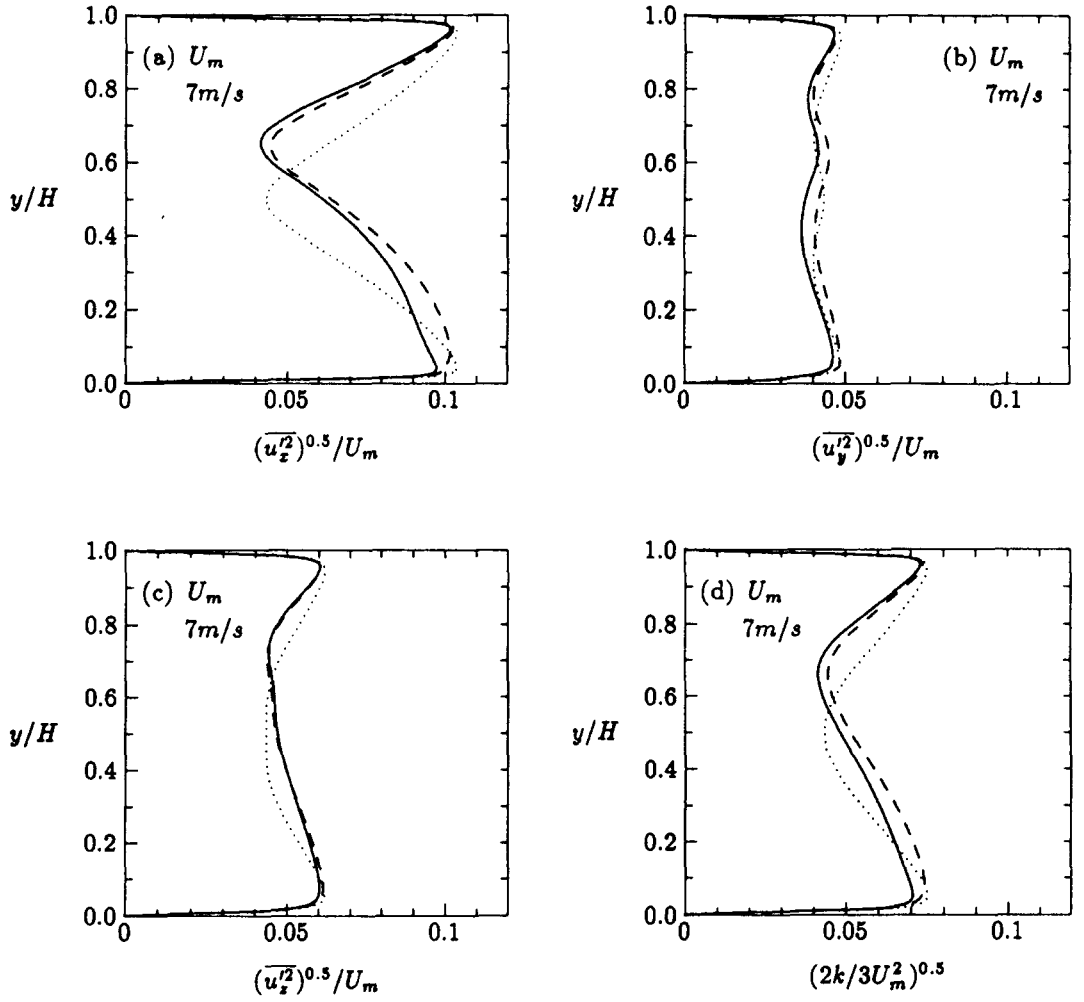

Figure 16. Air turbulence intensities. Simulations: . . ., $m_r = 0$; —, $m_r = 3$, $d = 1$ mm; – – –, $m_r = 3$, $d = 2$ mm.

and collisional stresses depend strongly on solids concentration. Therefore, it is not surprising to see that the particle stresses decrease with increasing elevation in a way somewhat similar to the variation of particle concentration shown in figure 2(a), (d).

Interestingly, the particle kinetic shear stress in figure 9(d), (h) is of the same order of magnitude as the total fluid shear stress as shown in figure 8. Furthermore, the particle kinetic shear stress actually changes sign at a certain location along the vertical axis. This behavior resembles the variation of the total fluid shear stress (or the Reynolds shear stress) across the channel height.

For dilute systems such as the ones being studied here, the particle collisional stresses are typically an order of magnitude lower than the particle kinetic stresses (see figures 9 and 10). This result however should not be viewed as to undermine the importance of interparticle collisions in sustaining a steady suspension. The main reason for such low particle collisional stresses is that the solids concentration is low. It is well known in the kinetic theory of granular flows that in dilute systems the dominant stresses are the kinetic ones rather than the collisional ones. For high solids concentrations the collisional stresses will dominate over the kinetic ones.

The distribution of the particle kinetic angular momentum flux (or sometimes called the kinetic couple stresses) is shown in figure 11. The major components are L_{kxz} and L_{kyz} while the minor ones are L_{kzx} and L_{kzy}. The other five components are typically two to three orders of magnitude smaller than the major ones. Moreover, in the present dilute systems the particle collisional couple stresses are at least one to two orders of magnitude smaller than the kinetic ones as shown in figure 12.

The effect of some interesting parameters other than the mass loading and the bulk gas velocity are examined in the present two-phase simulation as follows. Firstly, the coefficient of normal restitution is varied as shown in figure 13, where $e_p = 0.8$, 0.9 and 0.95 for fixed $\beta_0 = 0.4$ and $\mu_p = 0.47$. The particle concentration profile flattens monotonically with decreasing e_p as one might expect. However, the effect of e_p on the mean gas and particle velocities is rather complex due to the related factors such as the interfacial couplings, the particle rotations, and the interparticle collisions.

Figure 14 shows the variation of the friction coefficient with the particle concentration and the mean velocities. The solids concentration distribution levels off with decreasing friction due to the reduction in particle angular velocities and vertical Magnus lifts. When the walls and the particles are made frictionless, all the grains eventually deposit and roll along the bottom wall. This indicates that particle rotations play an equally important roll as do the interparticle collisions in sustaining a steady fully developed suspension in the grain inertia regime.

The effect of particle size on the flow properties are shown in figure 15. According to the present simulation, the mean particle Reynolds number for 2 mm diameter particles is found to be about 560. The significant effect in doubling the particle diameter is that the mean particle velocity, V_s/U_m is reduced by about 40%. In figure 16 it is interesting to note that in general the turbulence intensities are augmented due to the increase in particle diameter. These two predictions are consistent qualitatively with the experimental result obtained by Tsuji *et al.* (1982, 1984) in air–solid two-phase flows in a vertical pipe and a horizontal pipe.

7. CONCLUSION

A set of turbulent transport equations and a two-equation k–ϵ closure is used to model the fluid phase in a gas–solid suspension in this study. The trajectories and velocities of the solid particles are determined by integrating the particle equations of motion. A sticking–sliding collision model is employed for the particle–particle collisions and the particle–wall collisions. The simulation result for gas–solid flows in a horizontal channel shows that even though the suspension might be dilute with solids volume fraction of the order 10^{-3}, interparticle collision plays a critical role in maintaining a steady and fully developed suspension, and its effect should not be ignored. The effect of Magnus lift due to particle rotation is also important in suspending the solid phase. The incorporation of interparticle collisions, Magnus lift and a realistic sticking–sliding collision model in the simulation eliminates the need for any 'virtual wall' model.

In general, favorable agreement is found between the simulation result and the experimental measurements for the fluid pressure gradient and the distributions of mean fluid velocity, mean particle concentration and velocity in a horizontal channel-flow; detailed descriptions are given in the previous section. Interesting macroscopic properties such as mean particle angular velocity, air turbulence intensities, Reynolds stresses, translational and rotational granular temperatures, particle stresses and angular momentum fluxes are presented in the paper. Moreover, the effects of the coefficient of normal restitution, the friction coefficient and the particle size on the flow properties are studied. Such microscopic material properties have profound influence on the macroscopic flow properties of the two-phase gas–solid system in the inertia regime. The solid particles are suspended and transported along the channel by means of saltation and interparticle collisions as a result of the influxes of energy and momentum from the carrier fluid phase.

So far, we have used a mean coefficient of normal restitution e_p. In reality, e_p depends on the normal impact velocity. However, there are certain limitations to numerical simulations just like everything else. For example, if the coefficient of normal restitution of the flow particles is too low, the round-off errors in the double-precision floating point calculations can become large enough to cause unwarranted effects such as unrealistic collision time and overlapping of particles. Nonetheless, it seems worthwhile to implement an impact velocity dependent e_p for at least slightly inelastic materials in the present two-phase flow model.

Work is in progress to apply the present two-phase model to simulate gas–solid flows in horizontal pipes. Since two-phase flows in pipes are the predominant commercial means for material transport and processing, there are a few more detailed experimental investigations in pipe-flows than in channel-flows. The stress and turbulence intensities model of Nisizima and

Yoshizawa (1987) employed in the present study is only applicable to channel-flows so far. In order to study pipe-flows, a second-order turbulence closure model which will yield an appropriate set of anisotropic turbulence intensities will be utilized instead. As we have learned in the present channel-flow study, the interfacial coupling can strongly affect the fluid phase mean velocity and turbulence intensities. All the fluid and solid flow properties are intricately related. Therefore, a realistic description of the anisotropic turbulence intensities in the system is understandably critical in the study of turbulence modulation in fluid–solid flows.

Acknowledgements—This work was supported by a research grant from the Natural Science and Engineering Research Council of Canada.

REFERENCES

Clift, R. and Gauvin, W. H. (1971) Motion of entrained particle in gas stream. *Canadian J. Chem. Eng.* **49,** 439–448.

Crowe, C. T. (1982) Review: numerical models for dilute gas–particle flows. *J. Fluid Engr.* **104,** 297–303.

Crowe, C. T., Sharma, M. P. and Stock, D. E. (1977) The particle-source-in cell (PSI-cell) model for gas–droplet flows. *ASME, J. Fluids Eng.* **99,** 325–332.

Dennis, S. C. R., Singh, S. N. and Ingham, D. B. (1980) The steady flow due to a rotating sphere at low and moderate Reynolds numbers. *J. Fluid Mech.* **101,** 257–279.

Durst, F., Milojevic, D. and Schonung, B. (1984) Eulerian and Lagrangian predictions of particulate two-phase flows: a numerical study. *Appl. Math, Modeling* **8,** 101–115.

Elghobashi, S. E. (1994) On predicting particle-laden turbulent flows. *Appl. Sci. Res.* **52,** 309–329.

Elghobashi, S. E. and Truesdell, G. C. (1993) On the two-way interaction between homogeneous turbulence and dispersed solid particles. I: Turbulence modification. *Phys. Fluids* **A5,** 1790–1801.

Foerster, S. F., Louge, M. Y., Chang, H. and Allia, K. (1994) Measurements of collision properties of small spheres. *Phys. Fluids* **A6,** 1108–1115.

Frank, T., Schade, K. P. and Petrak, D. (1993) Numerical simulation and experimental investigation of gas–solid two-phase flow in a horizontal channel. *Int. J. Multiphase Flow* **19,** 187–198.

Goldsmith, W. (1960) *Impact: The Theory and Physical Behavior of Colliding Solids*. E. Arnold, New York.

Hanjalic, K. and Launder, B. E. (1976) Contribution towards a Reynolds stress closure for low-Reynolds number turbulence. *J. Fluid Mech.* **74,** 593–610.

Hinze, J. O. (1975) *Turbulence*. McGraw-Hill, New York.

Johnson, K. L. (1985) *Contact Mechanics*. Cambridge University Press, Cambridge.

Koch, D. L. (1990) Kinetic theory for a monodisperse gas–solid suspension. *Phys. Fluids* **A2,** 1711–1723.

Launder, B. E. and Spalding, D. B. (1974) The numerical computation of turbulent flows. *Computer Methods in Applied Mechanics and Eng.* **3,** 269–289.

Liu, H. S. (1995) Numerical simulation of turbulent gas–solid flows in horizontal channels. M.A.Sc. dissertation, Technical University of Nova Scotia, Canada.

Louge, M. Y., Mastorakas, E. and Jenkins, J. T. (1991) The role of particle collisions in pneumatic transport. *J. Fluid Mech.* **231,** 345–359.

Lourenco, L. and Essers, J. A. (1983) Computation of turbulent gas–particle suspension flows in channels. Lecture Series 1983–04, von Karman Institute for Fluid Dynamics.

Lourenco, L., Reithmuller, M. L. and Essers, J. A. (1983) The kinetic model for gas particle flow and its numerical implementation. In *Proc. Intl Conf. on the Physical Modelling of Multiphase Flow*, pp. 501–525. BHRA Fluid Engineering, Cranfield, UK.

Lun, C. K. K. (1991) Kinetic theory for granular flow of dense, slightly inelastic, slightly rough spheres. *J. Fluid Mech.* **233,** 539–559.

Lun, C. K. K. and Bent, A. A. (1994) Numerical simulation of inelastic frictional spheres in simple shear flow. *J. Fluid Mech.* **258,** 335–353.

Lun, C. K. K. and Savage, S. B. (1987) A simple kinetic theory for granular flow of rough, inelastic, spherical particles. *J. Appl. Mech.* **54,** 47–53.

Lun, C. K. K., Savage, S. B., Jeffrey, D. J. and Chepurniy, N. (1984) Kinetic theories for granular flow: inelastic particles in Couette flow and slightly inelastic particles in a general flowfield. *J. Fluid Mech.* **140,** 223–256.

Maw, N., Barber, J. R. and Fawcett, J. N. (1976) The oblique impact of elastic spheres. *Wear* **38,** 101–114.

Maw, N., Barber, J. R. and Fawcett, J. N. (1981) The role of elastic tangential compliance in oblique impact. *Trans. ASME F: J. Lubrication Technol.* **103,** 74–80.

Mei, R. (1992) An approximate expression for the shear lift force on a spherical particle at finite Reynolds number. *Int. J. Multiphase Flow* **18,** 145–147.

Nisizima, S. and Yoshizawa, A. (1987) Turbulent channel and Couette flows using an anisotropic k–ϵ model. *AIAA J.* **25,** 414–420.

Oesterle, B. and Petitjean, A. (1993) Simulation of particle-to-particle interactions in gas–solid flows. *Int. J. Multiphase Flow* **19,** 199–211.

Oesterle, B., Dinh Tri, B. and Vial, J. (1991) Measurements of lift and torque on a rotating sphere at intermediate Reynolds numbers. *Mech. Res. Commun.* **18,** 145–150.

Patankar, S. V. (1980) *Numerical Heat Transfer and Fluid Flow*. Hemisphere, Washingon, DC.

Rizk, M. A. and Elghobashi, S. E. (1989) A two-equation turbulence model for dispersed dilute confined two-phase flows. *Int. J. Multiphase Flow* **15,** 119–133.

Rubinow, S. I. and Keller, J. B. (1961) The transverse force on a spinning sphere moving in a viscous fluid. *J. Fluid Mech.* **11,** 447–459.

Saffman, P. G. (1965) The lift on a small sphere in a slow shear flow. *J. Fluid Mech.* **22,** 385–400.

Saffman, P. G. (1968) Corrigendum to "The lift on a small sphere in a slow shear flow". *J. Fluid Mech.* **31,** 624.

Sommerfeld, M. (1992) Modeling of particle-wall collisions in confined gas–particle flows. *Int. J. Multiphase Flow* **18,** 905–926.

Tsuji, Y. and Morikawa, Y. (1982) LDV measurements of an air–solid two-phase flow in a horizontal pipe. *J. Fluid Mech.* **120,** 385–409.

Tsuji, Y., Morikawa, Y. and Mizuno, O. (1985) Experimental measurement of the Magnus force on a rotating sphere at low Reynolds numbers. *ASME, J. Fluids Eng.* **107,** 484–488.

Tsuji, Y., Morikawa, Y., Tanaka, T., Nakatsukasa, N. and Nakatani, M. (1987) Numerical simulation of gas–solid two-phase flow in a two-dimensional horizontal channel. *Int. J. Multiphase Flow* **13,** 671–684.

Tsuji, Y., Morikawa, Y. and Shiomi, H. (1984) LDV measurements of an air–solid two-phase flow in a vertical pipe. *J. Fluid Mech.* **139,** 417–434.

APPENDIX A

Magnus Lift Coefficient

Rubinow and Keller (1961) found analytically that for $\mathrm{Re_p} < 1$, the Magnus lift coefficient is given by

$$C_{\mathrm{LM}} = \frac{\omega d}{v}\,[1 + O(\mathrm{Re_p})],$$

and the drag coefficient C_{D} is independent of the nondimensional rotational speed, $\omega d/v$. The quantities ω and v are the particle angular and translational speeds, respectively. Oesterle *et al.* (1991) measured the Magnus lift on a rotating sphere for $10 < \mathrm{Re_p} < 60$, and they proposed that the lift coefficient may be expressed as

$$C_{\mathrm{LM}} = (0.35 \pm 0.1)\,\frac{\omega d}{v}.$$

For $550 < Re_p < 1600$, Tsuji *et al.* (1985) inferred from their experimental data the correlation

$$C_{LM} = (0.2 \pm 0.05)\frac{\omega d}{v}.$$

Utilizing the above result, one may deduce the following correlation for the Magnus lift coefficient

$$C_{LM} = \frac{\omega d}{v} \quad (Re_p \leqslant 1)$$

$$C_{LM} = \frac{\omega d}{v}(0.178 + 0.822Re_p^{-0.522}) \quad (1 < Re_p < 1000)$$

which is applicable for a wider intermediate range of Re_p than the previous ones. Figure A1 shows the comparison of the correlation with the experimental data of Oesterle *et al.* (1991) and Tsuji *et al.* (1985).

APPENDIX B

Solid Phase Statistical Method

For a two-dimensional fully developed flow in a horizontal channel, the mean particle properties only vary in the vertical direction. The simulated control volume is partitioned into n number of horizontal strips across the channel. On the basis of the integrals for transport properties in the kinetic theories (Lun 1991; Lun and Savage 1987), one can deduce an equivalent set of discrete

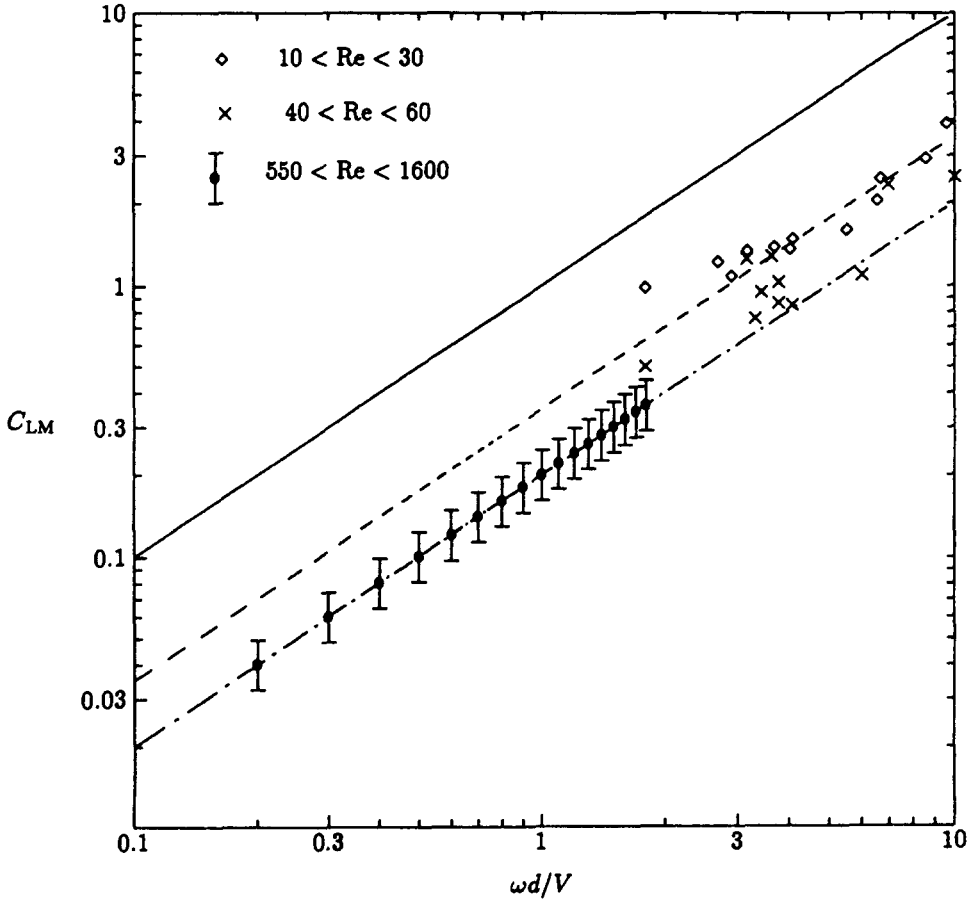

Figure A1. Lift coefficient versus dimensionless angular speed. Present correlation: —, Re = 1; – – –, Re = 20; – · – · –, Re = 1000. Experimental data: ◇, ×, Oesterle *et al.* (1991); ●, Tsuji *et al.* (1985).

formulae for determining the distribution of macroscopic properties such as mean velocity, concentration and stresses for the solid particles in the system. Let V_{ci} be the volume of the ith strip and N_i be the number of particles inside, then the volume fraction α_i, mean velocity $\mathbf{V}_i$, and mean angular velocity $\mathbf{\Omega}_i$ of the particles in the ith strip are

$$\alpha_i = \frac{\pi d^3 N_i}{6 V_{ci}}$$

$$\mathbf{V}_i = \frac{1}{N_i} \sum_j \mathbf{v}_j$$

$$\mathbf{\Omega}_i = \frac{1}{N_i} \sum_j \boldsymbol{\omega}_j$$

where Σ_j represents the sum over all the particles inside the ith strip.

The square of the mean intensity of translational fluctuation velocities in each strip is sometimes called the translational granular temperature since $T_t = \langle \mathbf{v}' \cdot \mathbf{v}' \rangle / 3$, and each component is given as

$$\langle \mathrm{v}_\beta'^2 \rangle_i = \frac{1}{N_i} \sum_j \mathrm{v}_{\beta j}' \mathrm{v}_{\beta j}'$$

where the subscript β can represent the x-, y- or z-directions. The angular brackets for particle properties represents long time ensemble average. Similarly, the square of the mean intensity of rotational fluctuation velocities or the rotational granular temperature is defined as

$$T_r = \frac{\mathbf{I}}{3 m_p} \langle \boldsymbol{\omega}' \cdot \boldsymbol{\omega}' \rangle.$$

The distribution of the translational granular temperature T_t and the rotational granular temperature T_r may be written, respectively, as

$$T_{ti} = \frac{1}{3N_i} \sum_j \mathbf{v}_j' \cdot \mathbf{v}_j'$$

and

$$T_{ri} = \frac{K_r}{12 N_i} \sum_j \boldsymbol{\omega}_j' \cdot \boldsymbol{\omega}_j'.$$

Other interesting flow properties such as particle stresses $\mathbf{P}_k$ and $\mathbf{P}_c$, and particle couple stresses (or angular momentum fluxes) $\mathbf{L}_k$ and $\mathbf{L}_c$, are useful in understanding the interactions of particles in the solid phase, and they may be expressed as

$$\mathbf{P}_{ki} = \frac{\pi d^3 \rho_p}{6 V_{ci}} \sum_j \mathbf{v}_j' \cdot \mathbf{v}_j'$$

$$\mathbf{P}_{ci} = \frac{d}{V_{ci} \Delta t} \sum_j \mathbf{J}_j \mathbf{K}_j$$

$$\mathbf{L}_{ki} = \frac{I}{V_{ci}} \sum_j \mathbf{v}_j' \cdot \boldsymbol{\omega}_j'$$

$$\mathbf{L}_{ci} = \frac{d^2}{2 V_{ci} \Delta t} \sum_j \mathbf{K}_j (\mathbf{J}_j \times \mathbf{K}_j)$$

where the subscripts k and c denote kinetic and collisional quantities, respectively. For example, the kinetic stresses $\mathbf{P}_k$ represent the rate of linear momentum transfer per unit area due to the streaming motion of particles. The collisional stresses $\mathbf{P}_c$ depict the rate of linear momentum transfer per unit area due to the exchange of linear momentum through interparticle collisions. Similar descriptions can be said about the couple stresses $\mathbf{L}_k$ and $\mathbf{L}_c$.